Remote Sensing of Environment 251 (2020) 112104

Contents lists available at ScienceDirect

Remote Sensing of Environment

journal homepage: www.elsevier.com/locate/rse

Estimating lake temperature profile and evaporation losses by leveraging MODIS LST data

Gang Zhao[a], Huilin Gao[a,*], Ximing Cai[b]

[a] Zachry Department of Civil and Environmental Engineering, Texas A&M University, College Station, TX 77843, USA
[b] Department of Civil and Environmental Engineering, University of Illinois at Urbana-Champaign, Urbana, IL 61801, USA

ARTICLE INFO

Keywords:
Evaporation
Heat storage
Lake temperature profile
Water surface temperature

ABSTRACT

Global lake evaporation is a critical component of the terrestrial water cycle. Accurate quantification of lake evaporation dynamics is of high importance for understanding lake energy budgets, land-atmosphere interactions, as well as regional water availability. However, the accurate quantification of lake evaporation has been hindered by the complexity involved with addressing the heat storage of water bodies. In this study, a new model—the Lake Temperature and Evaporation Model (LTEM)—was developed to simulate lake water temperature profiles, which were then used to calculate heat storage changes and evaporation rates. Inputs for the LTEM include the meteorological and bathymetric data, as well as the Moderate Resolution Imaging Spectroradiometer (MODIS) water surface temperature (WST)—which is the land surface te`mperature (LST) over water. The MODIS WST was leveraged to constrain the hydrodynamic simulations. Model results over 11 lakes around the world show robust performance of LTEM. The long term average temperature biases range from -0.5 °C to 0.5 °C, and the evaporation rate biases range from -0.19 mm/day to 0.28 mm/day. In particular, it is found that LTEM significantly improves the simulation of the seasonality of lake evaporation rates. The validation results suggest that the averaged coefficient of determination (R^2) for the evaporation rate is 0.84, which is 0.28 higher than that obtained when the conventional Penman equation (without heat storage) is used. The volumetric evaporation time series was then calculated as a product of the monthly evaporation rate and lake surface area (derived from MODIS near-infrared image classifications). This study provides an end-to-end framework for quantifying volumetric evaporation for the world's lakes and reservoirs. It also provides the capability to investigate the thermal dynamics of lake systems, and thus can benefit the various water resources applications across scales.

1. Introduction

Globally, the total open water area of the 1.42 million lakes/reservoirs is estimated to be about 2.67 × 10^6 km^2 (Messager et al., 2016). This large area leads to massive volumetric evaporative losses (Zhao and Gao, 2019). Meanwhile, these losses are sensitive to the changing climate since the evaporation process of these open water surfaces are energy limited (Brutsaert and Parlange, 1998; Wang et al., 2018). Although lake evaporation quantification is critical for water resources management (Wurbs and Ayala, 2014), climate modeling (Subin et al., 2012), ecosystem protection (Gianniou and Antonopoulos, 2007), and renewable energy generation (Cavusoglu et al., 2017), we still lack an accurate and robust quantification method to estimate volumetric evaporation—especially at a large scale (Friedrich et al., 2018).

Despite the fact that the evaporation process occurs only on the skin layer (~10 μm) of the water body, its magnitude is affected not only by the interactions between the atmosphere and the skin layer, but also between the skin layer and the water column (Hostetler and Bartlein, 1990). The former interaction is governed by four primary meteorological variables: solar radiation, atmospheric humidity, air temperature, and wind speed (McVicar et al., 2012); while the latter is controlled by the energy stored in the water body (de Bruin, 1982). Penman (1948) developed the first combination equation for calculating the open water evaporation rate. The Penman equation has been widely used in open water evaporation studies (Linacre, 1993; Terzi et al., 2006) and has been modified for use under varying conditions, including vegetated surfaces (Monteith, 1965) and advection free conditions (Priestley and Taylor, 1972; Morton, 1983). Compared to the energy balance or bulk aerodynamic evaporation assessment methods,

* Corresponding author at: Zachry Department of Civil and Environmental Engineering, Texas A&M University, College Station, TX 77843-3136, USA
E-mail address: hgao@civil.tamu.edu (H. Gao).

https://doi.org/10.1016/j.rse.2020.112104
Received 8 May 2020; Received in revised form 2 August 2020; Accepted 14 September 2020
Available online 24 September 2020

the Penman equation combines these two aspects to produce reliable evaporation rate estimates based on standardized meteorological data (McMahon et al., 2013). Because of the difficulties involved with measuring/estimating the heat storage changes of a water body, the Penman equation is only appropriate for quantifying the evaporation rates of shallow water bodies where the heat storage effect can be neglected (Vallet-Coulomb et al., 2001; Valiantzas, 2006; Sima et al., 2013). However, for deep lakes (> 10 m), heat storage changes can be equivalent to more than 50% of the net radiation (Allen and Tasumi, 2005) and lead to a significant shift of evaporation seasonality (Blanken et al., 2011; Moreo, 2015; Zhao and Gao, 2019).

The heat storage change, which is defined as the energy changes of the entire water body per unit area, can be calculated using the temperature profiles from two consecutive time steps (Gianniou and Antonopoulos, 2007). Based on this definition, heat storage changes can be obtained through observational or modeling methods. For example, a commonly used evaporation rate estimation method—the Bowen ratio energy budget (BREB) method—calculates heat storage changes from the observed water temperature profile (Stannard and Rosenberry, 1991; Lenters et al., 2005a; Elsawwaf et al., 2010). However, this method requires frequent recordings of water temperature at multiple depths, and thus is very labor- and time- intensive.

Modeling heat storage changes can be achieved by several methods: 1) simple regression between heat storage changes and net radiation (Duan and Bastiaanssen, 2015); 2) equilibrium temperature simulation (Finch, 2001; McJannet et al., 2008; Zhao and Gao, 2019); and 3) water temperature profile simulation (Hostetler and Bartlein, 1990). The simple regression method uses a hysteresis function to relate heat storage changes and net radiation, and thus may result in large uncertainties. The equilibrium temperature method is physically-based, with an assumption that the water body is well-mixed. However, this assumption neglects the vertical temperature gradient of the water body and thus introduces uncertainties—especially for deep (> 10 m) lakes (Blanken et al., 2000). The last method aims to continuously simulate the water temperature profiles through numerical modeling (e.g., hydrodynamic models). It has shown a great potential due to the development of accurate modeling approaches (Subin et al., 2012).

One-dimensional (1-D) hydrodynamic models have demonstrated the capability of simulating water temperature profiles and dynamics (Bowling and Lettenmaier, 2010; Subin et al., 2012). The driving assumption of the 1-D model is horizontal homogeneity, which is commonly valid due to the vertical density gradient (Perroud et al., 2009). Several types of 1-D models have been developed, including: 1) simple 2-layer (mixed-thermocline) models such as FLake (Kirillin et al., 2011); 2) radiation-diffusion models (Hostetler and Bartlein, 1990, hereafter referred to as the Hostetler Model); and 3) turbulence models (Hamilton and Schladow, 1997; Goudsmit et al., 2002). Results from model inter-comparisons have been reported in Perroud et al. (2009) and Stepanenko et al. (2010). Due to its solid physical basis and computational efficiency (Stepanenko et al., 2013), the Hostetler Model has been widely employed for lake temperature profile simulations (e.g., Bowling and Lettenmaier, 2010).

With any of the methods described above, water temperature profile simulations—like other hydrodynamic models which use a consecutive numerical method—tend to have reduced accuracies as the simulation uncertainties propagate with time (Samaniego et al., 2017). This issue can be alleviated by incorporating satellite temperature measurements into the models. Thermal sensors such as the Moderate Resolution Imaging Spectroradiometer (MODIS) and the Thermal Infrared Sensor (TIRS) can measure the land surface temperature (LST) with high accuracy (Wan, 2014). With regard to water surface, LST represents the water surface temperature (WST) of the skin layer (~10 μm)—which provides an ideal boundary condition for lake temperature profile simulations. Compared to in-situ observations, remotely sensed WST data are advantageous in terms of temporal continuity, global coverage, cost efficiency, and representation of spatial heterogeneity (Coll et al., 2009; Wang et al., 2007). However, to our best knowledge there have been no studies which have attempted to use a hydrodynamic model to leverage these globally available data for simulating lake water temperature profiles and calculating evaporation losses.

Therefore, the overarching objective of this study was to develop a modeling framework to leverage remotely sensed WST data for estimating lake temperature profiles and evaporation more accurately. A new model—the Lake Temperature and Evaporation Model (LTEM)—was developed for this purpose. In LTEM, MODIS WST data were employed to constrain the modified Hostetler Model for calculating lake water temperature profiles. The temperature profiles were then used to calculate lake heat storage changes and evaporation rates. Lastly, the volumetric evaporation time series was calculated as the product of the monthly evaporation rate and lake surface area (derived from MODIS near-infrared image classifications) (Section 2). The framework was validated over 11 lakes that have either in-situ temperature or evaporation rate data (Section 3 and Section 4), and its potential contributions and uncertainties are discussed in Section 5.

2. Data and methods

2.1. Data for volumetric evaporation calculation

The datasets used in this study, which are all available in the public domain, are summarized in Table 1. Specifically, the MODIS 250 m 8-day global surface reflectance products (i.e., MOD09Q1 and MYD09Q1) were used to extract lake surface area time series values. The MODIS 1km 8-day global LST products (i.e., MOD11A2 and MYD11A2) over lakes were used for deriving the WST time series. The global reanalysis dataset, TerraClimate, was used as the meteorological forcing data to drive the LTEM. Built upon the widely used Climate Research Unit 4.0 and Japanese 55-year Reanalysis data, TerraClimate provides monthly solar radiation, air temperature, vapor pressure, and wind speed data from Jan 1958 to Dec 2018, with a spatial resolution of 1/24 degree (Abatzoglou et al., 2018). Detailed discussion about the other ancillary datasets included in Table 1 (e.g., HydroLAKES) can be found in the following text in this section.

Table 1
Data used for lake surface area and WST extraction.

Data	Spatial resolution	Temporal resolution	Purpose	Reference
HydroLAKES	shapefile	Time-invariant	Lake mask	Messager et al., 2016
OpenStreetMap	shapefile	Time-invariant	Lake mask	Haklay and Weber, 2008
Terra surface reflectance (MOD09Q1)	250 m	8-day	Water area extraction	Vermote et al., 2015
Aqua surface reflectance (MYD09Q1)	250 m	8-day	Water area extraction	Vermote et al., 2015
Global surface water dataset (GSWD) occurrence	30 m (resample to 250 m)	Time-invariant	Water area enhancement	Pekel et al., 2016
Terra LST (MOD11A2)	1 km	8-day	WST extraction	Wan, 2014
Aqua LST (MYD11A2)	1 km	8-day	WST extraction	Wan, 2014
GloboLakes lake surface temperature	1/20°	1-day	WST bias-correction	Carrea and Merchant, 2019
TerraClimate	1/24°	1-month	Meteorological forcing data for LTEM	Abatzoglou et al., 2018

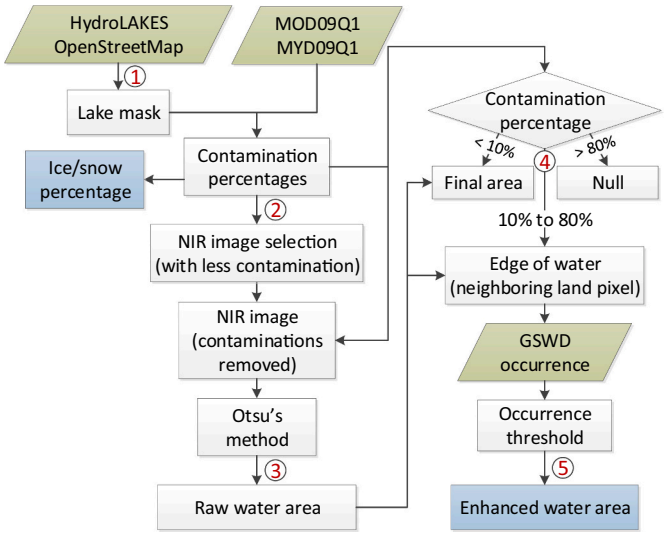

Fig. 1. Flowchart for generating the water area from the MODIS surface reflectance product. "Null" means that the image has been rejected, in which case the area is calculated through interpolation. The numbers show the processing steps. Green and blue colors indicate input and output, respectively.

2.2. Generating lake surface area time series

Lake surface area time series were generated from MODIS image classifications. Instead of using water indices (e.g., normalized difference water index), only the near-infrared (NIR) band (841-876 nm) was selected for extracting the water area. This was based on two considerations: First, NIR has been commonly used for classifying water, as it is strongly absorbed by water (Wozniak and Dera, 2007). Second, NIR is one of only two bands on the MODIS sensor that have a high spatial resolution (250 m). Fig. 1 shows the flowchart of the algorithm. Using Lake Mead as an example (Fig. 2), details about each of these steps are described in the following paragraphs.

1) Lake mask generation: For a given lake of interest, the shapefiles from HydroLAKES and OpenStreetMap were compared and the one with the larger area was selected. The lake mask was then generated by buffering the selected shapefile outward by 1000 m. This buffering approach allowed the mask to include all possible water pixels (Gao et al., 2012). By leveraging these two datasets, the possible underestimations from either of them can be eliminated. All of the subsequent steps were executed within the masked region.
2) Selection of NIR images: For each 8-day period, the contamination percentages (CPs) were calculated for NIR images from both Terra (MOD09Q1) and Aqua (MYD09Q1) reflectance products using their respective quality assurance (QA) band. A pixel that was covered by cloud, cloud shadow, or snow/ice was regarded as contaminated. The image with less contamination was selected (Fig. 2a)—and each of its contaminated pixels was set to a default "no data" value (Fig. 2b). Instead of combining these two, using the less-contaminated LST image can reduce the computational cost while still producing satisfactory water classification results due to the implementation of the following image enhancement algorithm. In addition, the snow/ice area percentage was estimated from the MOD09Q1/MYD09Q1 QA band over the enhanced water area to facilitate the volumetric evaporation calculation (Section 2.5) (Zhang and Pavelsky, 2019).
3) Raw water area classification: The Otsu thresholding method (Otsu, 1979; Lu et al., 2017) was applied to the selected NIR image for classifying the raw water area (Fig. 2c).
4) Enhancement decision: If the CP of the image (from Step 2) was less than 10%, the image was regarded as clear and the raw water area was deemed final. If the CP was larger than 80%, the image was considered to be severely contaminated and thus discarded. In this case, the missing water area value was estimated by interpolation. Otherwise (10% ≤ CP ≤ 80%), an image enhancement algorithm was performed.
5) Image classification enhancement: Adopted after Zhang et al. (2014), the basis for this procedure is that the water boundary should be consistent with the long-term occurrence image. Using the water occurrence image as a reference, the coastline in the contamination-free area can be extrapolated to cover the entire lake. Compared to Zhao and Gao (2018), which used an empirical parameter to define the occurrence threshold, the proposed algorithm in this study is more physically-based and is parameter-independent. First, the edge pixels (i.e., coastline) located between water and not-water areas were identified (Fig. 2d). By overlapping these edge pixels with the occurrence image (Fig. 2e), a cumulative distribution function (CDF) of the occurrence values for these edge pixels was created. Then, the occurrence value which corresponded to a CDF of 0.9 was selected as the threshold. This threshold was used to reduce the impact of possible misclassified pixels in the raw water area. Finally, all of the contaminated pixels ("no data" pixels after Step 2) in the raw water area that satisfied the condition [occurrence value ≥ threshold] were reclassified as water (Fig. 2f).

After applying the above steps to each selected MODIS NIR image, an area time series with an 8-day interval was generated. Although the quality control processes (Steps 2 and 4) were implemented and the contaminated images were corrected (Step 5), outliers still existed in the area time series for some lakes. This could be attributed to misclassifications with the raw water area, which can directly affect the performance of the enhancement algorithm, and/or to errors associated with the MODIS QA band. In addition, area values for some months were missing due to the removal of severely contaminated images. To address this issue, an outlier removal and gap interpolation procedure was adopted from Zhao and Gao (2018). First, the biases were calculated by subtracting the time series using a 7-timestep moving average. The outliers were identified as having a bias value greater than three times the standard deviations (of the bias time series). Then these outliers were removed, and the gaps were interpolated using their neighboring values. This scheme was executed until there were no more outliers identified.

2.3. Generating water surface temperature time series

The 8-day WST time series values were extracted from the MODIS LST products (i.e., MOD11A2 and MYD11A2) and bias-corrected using the GloboLakes WST climatology (Carrea and Merchant, 2019). As reported in several regional studies (Crosman and Horel, 2009; Chavula et al., 2009; Song et al., 2016; Wan et al., 2017), MODIS based WST tends to have biases toward cooler temperatures (~1.5 °C) when compared to in-situ buoy data. Rather than the skin effect, which typically ranges from 0 °C to 0.6 °C (Horrocks et al., 2003), this cooling bias is likely caused by a combination of several other factors—such as an underestimation of atmospheric attenuation, and/or an overestimation of surface emissivity (Crosman and Horel, 2009). The WST data from GloboLakes were measured by the (Advanced) Along-Track Scanning Radiometer and the Advanced Very-High-Resolution Radiometer, and its quality has been extensively validated using in-situ observations (Hook et al., 2003; MacCallum and Merchant, 2012; Wan et al., 2017). To confirm the possible cooling bias of MODIS WST—and to independently validate the quality of GloboLakes—we compared both WST products with in-situ data from the Global Lake Temperature Collaboration (GLTC; Sharma et al., 2015) for 21 lakes across the world (Supplementary data Fig. S1). It was found that MODIS WST has an average bias of -1.86 °C, while GloboLakes has an average bias of -0.10 °C.

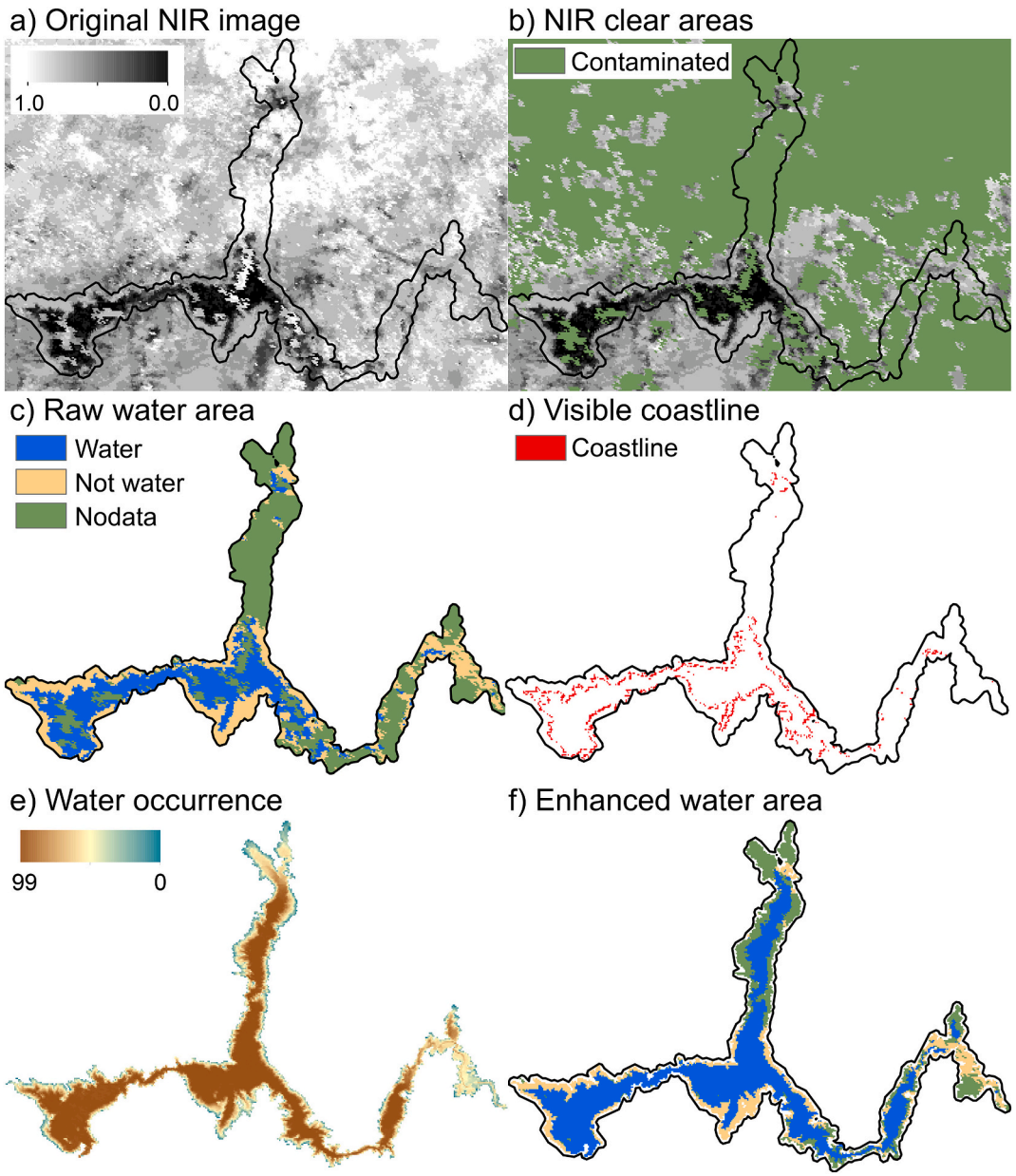

Fig. 2. Water area enhancement process for contaminated MODIS images. The Terra image collected on Jan 1, 2005 for Lake Mead in the USA was selected as an example.

Instead of using the GloboLakes WST products directly, we bias-corrected MODIS using GloboLakes. This is because GloboLakes only contains WST time series values for 979 lakes due to its coarse resolution (1/20°). This limited its global application, especially for small lakes. Meanwhile, the comparison between MODIS and GloboLakes suggests that the cooling bias for MODIS WST has clear regional and seasonal patterns (Supplementary data Fig. S2). Thus, when GloboLakes data were not available for a small lake, a nearby larger lake was used to approximate the climatological biases. It is worth noting that MODIS WST has its largest cooling biases from July to September (Supplementary data Fig. S3), which is consistent with the findings by Sharma et al. (2015) and Wan et al. (2017). The detailed WST time series generation was implemented in the following 4 steps:

1) Selection of LST images: For each 8-day time step, based on the selected NIR images (i.e., Step 2 in the area extraction processes), the LST images from the same satellite (MOD11A2 or MYD11A2) were adopted.
2) Calculation of the WST value: For each image, the LST pixel values (from both daytime and nighttime) were averaged over the raw water area (buffered inward by 750 m to remove possible mixed pixels). Since the daily temperature variations roughly follow a sinusoidal curve, the average of the MODIS daytime and nighttime temperatures (1:30/13:30 local time for Aqua and 10:30/22:30 for Terra) can effectively represent the mean daily temperature.
3) Outlier removal and gap filling: Outliers existed due to image contaminations and the misclassification of raw water areas. Thus, following the same method adopted by the area extraction processes, outliers within the WST time series were removed and the data gaps were filled via interpolation.
4) Bias correction: The monthly climatological biases were calculated for each lake as the difference between GloboLakes and the MODIS WST climatology. These bias values were then added to the MODIS WST time series to produce the bias-corrected results.

After all of the aforementioned computations were performed, the

8-day time series for lake surface area, the WST, and the ice/snow percentage were aggregated to a monthly time step that was consistent with the meteorological data and the evaporation rate estimation.

2.4. Calculating evaporation rate time series using LTEM

The evaporation rate calculation in LTEM is based on the Penman equation, with the wind function represented, after Zhao and Gao (2019) (Equation 1):

$$E = \frac{\Delta(R_n - G) + \gamma f(u)(e_s - e_a)}{\lambda_v(\Delta + \gamma)} \quad (1)$$

where E is the open water evaporation rate (mm·d^{-1}); Δ is the slope of the saturation vapor pressure curve (kPa·°C^{-1}); R_n is the net radiation (MJ·m^{-2}·d^{-1}); G is the heat storage change of the water body (MJ·m^{-2}·d^{-1}); γ is the psychrometric constant (kPa·°C^{-1}); $f(u)$ is the wind function that is dependent on lake fetch (MJ·m^{-2}·d^{-1}·kPa^{-1}) (McJannet et al., 2012); e_s is the saturated vapor pressure at air temperature (kPa); e_a is the air vapor pressure (kPa); and λ_v is the latent heat of vaporization (MJ·kg^{-1}). Because all of the other terms in the Penman equation are well formulated (Penman, 1948; Zhao and Gao, 2019), we focused on explaining the new approach for quantifying the heat storage change term that leverages MODIS WST data. The heat storage changes (G) can be calculated using temperature profile data of two consecutive time steps (Equation 2; Gianniou and Antonopoulos, 2007):

$$G = \frac{1}{A_s}\frac{\mathrm{d}}{\mathrm{d}t}\int_0^{D_t} \rho_{w,z,t} c_{w,z,t} A_{z,t} T_{z,t}\, \mathrm{d}z \quad (2)$$

where A_s is the surface area of the water body (m^2); t is the current time step (d); $\rho_{w,z,t}$ is the density of water at depth z and time t (kg·m^{-3}); $c_{w,z,t}$ is the specific heat of water at depth z and time t (J·kg^{-1}·°C^{-1}), $A_{z,t}$ is the water area at depth z and time t (m^2); $T_{z,t}$ is the water temperature at depth z and time t (°C); and D_t is the total depth of the water body at time t (m).

To simulate the temperature profile for each time step ($T_{z,t}$, $0 \le z \le D_t$ and $0 \le t \le END$) in LTEM, we integrated MODIS WST data into the 1-D Hostetler Model (Hostetler and Bartlein, 1990). In this subsection, we first explain the lake energy budget terms (2.4.1) and then the Hostetler Model (2.4.2), which were used to facilitate temperature profile and evaporation rate simulation in LTEM (2.4.3).

2.4.1. Lake energy budget terms

The evaporation process of a lake involves both energy fluxes at the water surface and energy transfer in the water body (Fig. 3).

For a water body, the net radiation (R_n, MJ·m^{-2}·d^{-1}) can be formulated after Equation 3:

$$R_n = K_{in} - K_{out} + L_{in} - L_{out} \quad (3)$$

where K_{in}, K_{out}, L_{in}, and L_{out} are surface incoming shortwave radiation (MJ·m^{-2}·d^{-1}), outgoing shortwave radiation (MJ·m^{-2}·d^{-1}), surface incoming longwave radiation (MJ·m^{-2}·d^{-1}), and outgoing longwave radiation (MJ·m^{-2}·d^{-1}), respectively. Among these terms, K_{in} can be directly adopted from meteorological forcing inputs, while the others are calculated. K_{out} can be calculated using the water surface albedo (α) following Equation 4 after Subin et al. (2012):

$$K_{out} = \alpha \cdot K_{in} = \frac{0.05}{\cos\theta_s + 0.15} \cdot K_{in} \quad (4)$$

where θ_s is the solar zenith angle (Zhao and Gao, 2019). L_{in} (MJ·m^{-2}·d^{-1}) and L_{out} (MJ·m^{-2}·d^{-1}) can be calculated using Equations 5 and 6 after the Stefan–Boltzmann Law:

$$L_{in} = \varepsilon_a \sigma (T_a + 273.15)^4 \quad (5)$$

$$L_{out} = \varepsilon_w \sigma (WST + 273.15)^4 \quad (6)$$

where ε_a is the emissivity of air with a cloudiness factor included (0-1; Zhao and Gao, 2019); ε_w is the emissivity of water (0.97); σ is the Stefan-Boltzman constant (4.9×10^{-9} MJ·m^{-2}·K^{-4}·d^{-1}); and T_a is the air temperature (°C).

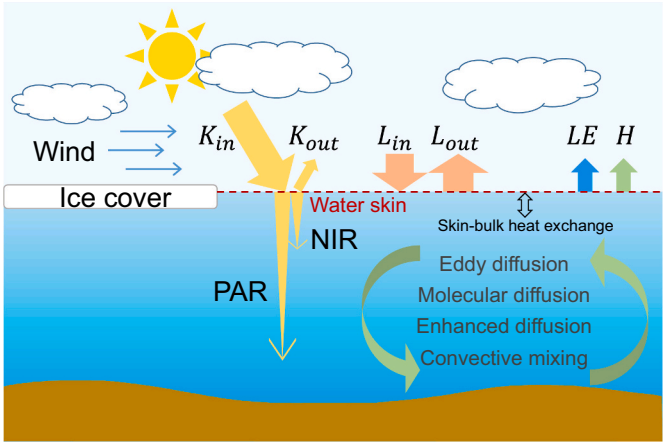

Fig. 3. Schematic of the Lake Temperature and Evaporation Model (LTEM) model, which involves both energy fluxes at the water surface and energy transfer in the water body. PAR and NIR represent photosynthetically active radiation and near infrared radiation, respectively. Definitions for other energy terms can be found in Equations 3 and 10.

The net shortwave radiation ($K_{in} - K_{out}$) penetrates the water column and is absorbed according to the Beer-Lambert Law. The net shortwave radiation is divided into photosynthetically active radiation (PAR) and near-infrared radiation (NIR). The transmitted shortwave energy at depth z (denoted as K_z) can be calculated after Equation 7 (Ingle Jr and Crouch, 1988):

$$K_z = (K_{in} - K_{out}) \cdot (\theta_{PAR} e^{-\lambda_{PAR} \cdot z} + \theta_{NIR} e^{-\lambda_{NIR} \cdot z}) \quad (7)$$

where θ_{PAR} and θ_{NIR} are the shortwave radiation fractions of PAR and NIR; and λ_{PAR} and λ_{NIR} are the light attenuation coefficients of PAR and NIR. After Escobedo et al. (2009), θ_{PAR} and θ_{NIR} are set to 0.54 and 0.46, respectively. λ_{NIR} is set to 1.4 m^{-1} after Bowling and Lettenmaier (2010). The λ_{PAR} value is provided by the user when direct light attenuation measurements are available, or it can be calculated from the Secchi depth measurement (Z_{sd}, in m) using Equation 8 (Devlin et al., 2008). Alternatively, λ_{PAR} can be empirically calculated using the lake average depth (D, in m) after Equation 9 (Håkanson, 1995; Bennington et al., 2014).

$$\lambda_{PAR} = exp(0.253 - 1.029 \cdot ln\, Z_{sd}) \quad (8)$$

$$\lambda_{PAR} = 1.1925 D^{-0.424} \quad (9)$$

Unlike shortwave radiation which can penetrate water, the incoming longwave radiation (L_{in}) is only absorbed by the water surface. Meanwhile, the surface also loses energy through outgoing longwave radiation (L_{out}), latent heat flux (LE, MJ·m^{-2}·d^{-1}), and sensible heat flux (H, MJ·m^{-2}·d^{-1}). In summary, for a given water body, the energy it recieves at each time step can be separated into two parts based on location: 1) the "penetrating" net shortwave radiation ($K_{in} - K_{out}$), and 2) the "surface" energy influx (EI_s) which is defined after Equation 10:

$$EI_s = L_{in} - L_{out} - LE - H \quad (10)$$

2.4.2. The Hostetler model

In this study, to facilitate the calculation of temperature profile, the modified Hostetler Model scheme was adopted from Bowling and Lettenmaier (2010) and Subin et al. (2012). The governing equation for water temperature profile is denoted as a partial differential equation (Equation 11):

$$\frac{\partial T_{z,t}}{\partial t} = \frac{1}{A_{z,t}}\frac{\partial}{\partial z}\left[A_{z,t}(\kappa_m + \kappa_{E,z,t} + \kappa_{en})\frac{\partial T_{z,t}}{\partial z}\right] + \frac{1}{A_{z,t}}\frac{1}{c_{w,z,t}}\frac{\partial (K_{z,t}A_{z,t})}{\partial z} \quad (11)$$

where $T_{z,\ t}$ is the water temperature at depth z and time t; κ_m is the molecular diffusivity (1.39×10^{-7} $m^2{\cdot}s^{-1}$); $\kappa_{E,\ z,\ t}$ and κ_{en} are the eddy and enhanced diffusivities, respectively ($m^2{\cdot}s^{-1}$); $K_{z,\ t}$ is K_z (Equation 7) at time t; and $A_{z,\ t}$ is the area at depth z and time t (which is calculated using the lake bathymetry). Following Hostetler and Bartlein (1990), $\kappa_{E,\ z,\ t}$ can be calculated after Equation 12:

$$\kappa_{E,z,t} = \frac{(\kappa \nu_s z/P_0)e^{-k_e z}}{1 + 37R_i^2} \quad (12)$$

where κ is the von Kármán constant (0.4); ν_s is the surface shear velocity (which depends on surface forcing and temperature; Vickers et al., 2015); P_0 is the neutral value of the turbulent Prandtl number (1.0); k_e is the Ekman profile parameter; and R_i is the gradient Richardson number. The detailed formulation for these parameters can be found in Hostetler and Bartlein (1990).

The enhanced diffusion is introduced by turbulence sources other than wind-driven eddies, such as surface water inflow/outflow, seiches, the horizontal temperature gradient, and aquatic life movement. κ_{en} can be written as Equation 13:

$$\kappa_{en} = \alpha_\kappa \bullet 1.04\times10^{-8}(N^2)^{-0.43} \quad (13)$$

where α_κ is the enhanced diffusion coefficient ($0 \le \alpha_\kappa \le 1000$; Bennington et al., 2014), and N^2 is the Brunt-Vaisala frequency (s^{-2}) (Fang and Stefan, 1996; Subin et al., 2012). The value of α_κ can be calibrated using temperature profile measurements (Ellis et al., 1991). In this study, we used an empirical value of 20 for α_κ to show the general applicability of the LTEM model. We did, however, test the sensitivity of α_κ (using Lake Mead as an example) to find its impacts on the temperature profile and the evaporation rate (Section 4.4).

For general Hostetler Model applications, the water temperature profiles are calculated after Equation 11 with $K_{in} - K_{out}$ and EI_s as energy inputs. Then, the convection is implemented from the top layer to the bottom according to the temperature-based density gradient. For instance, if an upper layer is denser than its adjacent lower layer (density calculated based on temperature), then these two layers will be mixed and the resulting thickness-weighted average temperature will be assigned to both of them. This convection process is executed until there is no inverse density gradient.

2.4.3. Lake temperature profile and evaporation simulation

The Hostetler Model can be used to recursively calculate $T_{z,\ t}$ ($0 \le z \le D_t$) if the external energy inputs at each time step (i.e., shortwave radiation, $K_{in} - K_{out}$, and surface influx, EI_s) are provided. However, conventional methods for quantifying LE and H contain large uncertainties—which makes it difficult to estimate EI_s at each time step.

To resolve this issue, we applied the MODIS WST at time t as a boundary condition to constrain the calculation of $T_{z,\ t}$. At time t, the known variables were $T_{z,\ t-1}$ ($0 \le z \le D_{t-1}$), $L_{in} - L_{out}$, and WST_t. An iterative solver (similar to a Kalman Filter) was developed in LTEM to calculate $T_{z,\ t}$. Before the calculation of temperature for each new time step, the lake depth (D_t) was calculated using the lake bathymetry and the remotely sensed lake area (Section 2.2). This lake depth was divided into layers using a layer thickness value (0.6 m was used for this study, but this can be set by users as needed). The process at each time step is summarized in the following 6 steps (and in the flowchart in Fig. 4):

1. Prior to the iteration at the current time step (t), it was first assumed that there is no heat storage effect in the Penman equation (i.e., $G = 0$ in Equation 1). Thus, an initial value of EI_s can be calculated, with $LE = \lambda_v E$ and H calculated after Equation 14 (with the same wind function as used in Equation 1):

$$H = \gamma f(u)(WST_t - T_a) \quad (14)$$

2. $T_{z,\ t}$ ($0 \le z \le D_t$) can then be calculated using the Hostetler Model based on $T_{z,\ t-1}$ ($0 \le z \le D_{t-1}$), along with $K_{in} - K_{out}$, EI_s, and the layer configuration derived from the lake bathymetry.
3. The remotely sensed skin temperature at time t (WST_t) was converted to the bulk temperature (T_t^{bulk}) by considering the cool-skin effect ($\Delta T_{skin,\ t}$) after Equation 15 (Artale et al., 2002). Compared to the more complex formulation provided by Fairall et al. (1996), the formulation by Artale et al. (2002) significantly simplifies the computation and still produces satisfactory outputs (Tu and Tsuang, 2005).

$$T_t^{bulk} = WST_t + \Delta T_{skin,t} = WST_t + \frac{EI_s/0.0864\bullet\delta}{k} \quad (15)$$

where δ is the thickness of the skin layer (m), and k is the thermal conductivity of water ($W{\cdot}m^{-1}{\cdot}K^{-1}$). This bulk temperature represents the water temperature of the first water layer right beneath the skin layer.

4. If the simulated $T_{0,\ t}$ was different from the remotely sensed T_t^{bulk}—which indicated that the initial EI_s was biased— Δ_{EI} was subtracted from EI_s, and Steps 2 and 3 were repeated. This iteration was executed until $|T_{0,\ t} - T_t^{bulk}|$ was smaller than ϵ (e.g., 0.01 °C). Δ_{EI} is defined as:

$$\Delta_{EI} = lr\bullet(T_{0,t} - T_t^{bulk}) \quad (16)$$

where lr is the learning rate (e.g., π, or other irrational numbers).

5. After the model had converged (i.e., $|T_{0,\ t} - T_t^{bulk}| < \epsilon$), the heat storage change (G) was calculated following Equation 2 (Gianniou and Antonopoulos, 2007).
6. The evaporation rate (E) was then calculated using the Penman equation (with the wind function represented) after Zhao and Gao (2019) (Equation 1).

In summary, by implementing the above iterations, the water temperature profile at the previous time step ($T_{z,\ t-1}$)—and the water skin temperature at the current time step (WST_t)—can lead to the water temperature profile at the current time step ($T_{z,\ t}$). To get a stable temperature profile time series, LTEM can be spun up for a sufficient period of time (e.g., 24-months), and then normal simulations can be started. In this study, we implemented LTEM at a monthly time step—meaning that we solved the temperature profile for each month, and then calculated the evaporation rate for each month. It is worth noting, that LTEM can be implemented at a finer time step (e.g., daily or weekly) if higher temporal resolution meteorological data (e.g., Daymet) and WST data (e.g., derived from ECOSTRESS) are available.

2.5. Calculating volumetric evaporation

After calculating the evaporation rate time series, the volumetric evaporation can be inferred by multiplying the evaporation rate with the surface area (with the fraction of ice/snow cover excluded) (Equation 17).

$$V_E = E \times A \times (1 - r_{ice}) \quad (17)$$

where A is the enhanced water area (km^2), and r_{ice} is the fraction of ice/snow coverage. As described in Section 2.2, r_{ice} is calculated by dividing the area of snow/ice pixels (from MODIS QA band) with the enhanced water area. Because the portion of evaporation from snow/ice (i.e., ice sublimation) can be approximated as zero, the snow/ice area was not considered when the volumetric evaporation was calculated.

3. Algorithm test sites

The performance of LTEM was evaluated over 11 lakes where

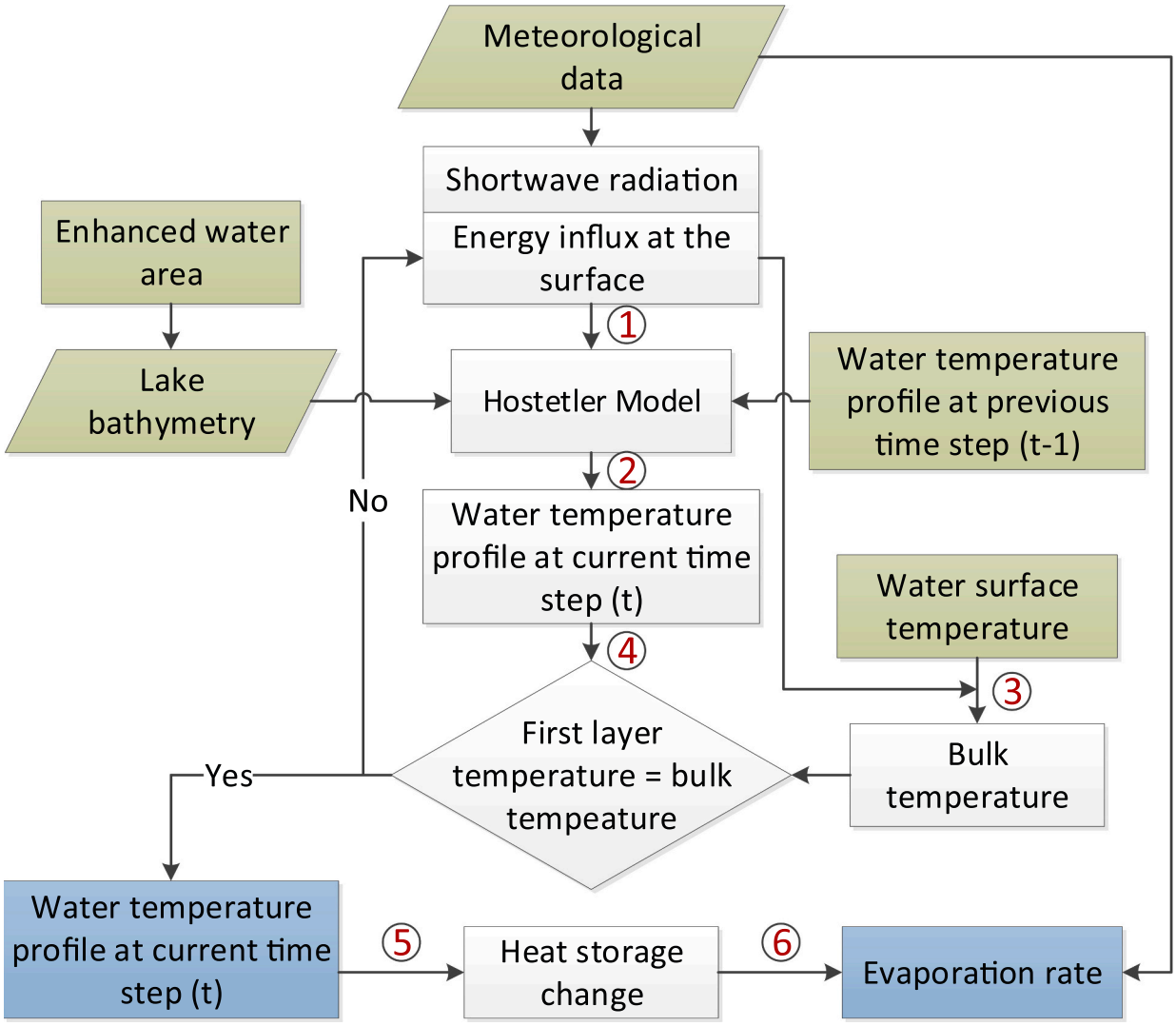

Fig. 4. Flowchart for calculating the water temperature profile from $t-1$ to t, and the heat storage and evaporation rates. Green and blue colors indicate inputs and outputs, respectively.

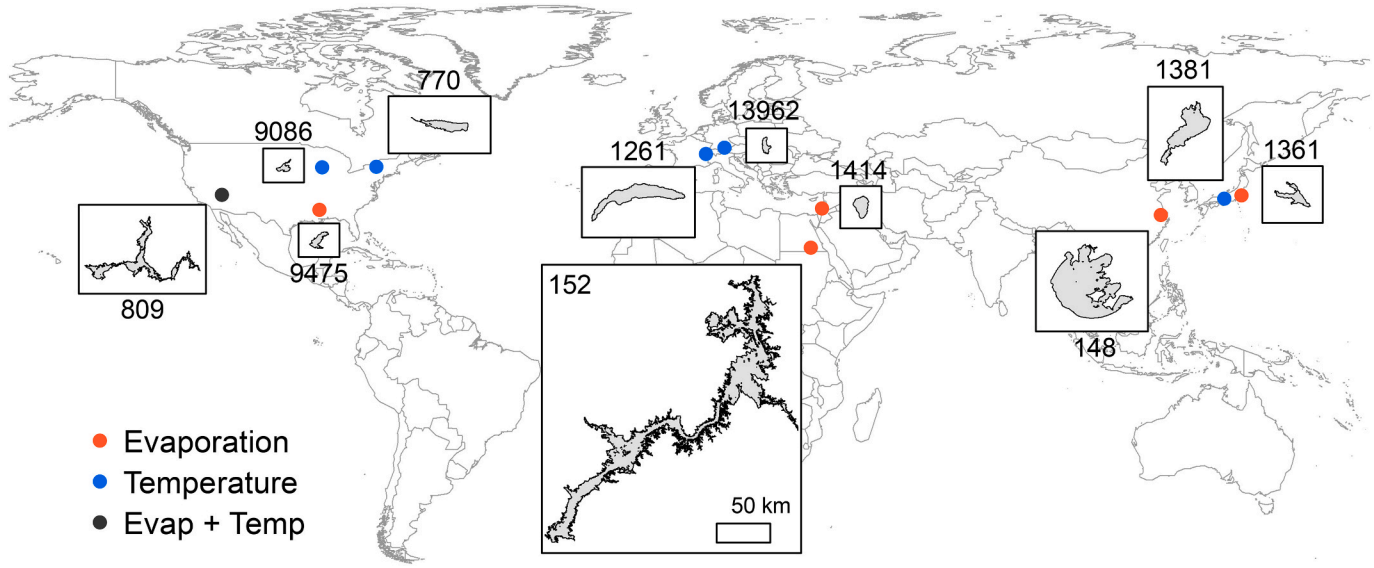

Fig. 5. The 11 lakes selected for evaluating LTEM. The scale indicated for Lake Nasser also applies to the other lakes. The number for each lake is the HydroLAKES ID as listed in Table 2.

Table 2
Eleven global lakes, with the in-situ observed temperature profile and evaporation rate. Note that Lake Mead (HydroLAKES ID 809) has two rows for temperature and evaporation rate observations.

HydroLAKES ID	Lake	Region	Location (Lat, Lon)	Elevation (m)	Average depth (m)	Average area (km^2)	T/E	E method	Data period	Reference
148	Lake Taihu	East Asia	31.1, 120.5	0	2.2	2329	E	EC	Jul 2010 – Aug 2012	Wang et al., 2014
152	Lake Nasser	Africa	23.9, 32.9	179	30	5385	E	BREB	Jan 2000 – Jul 2004	Elsawwaf et al., 2010
770	Oneida Lake	North America	43.3, -76.2	112	11	207	T	/	Feb 2000 – Dec 2014	Rudstam, 2015
809	Lake Mead	North America	36.0, -114.7	372	63	580	E, T	EC	Mar 2010 – Apr 2015 for E; Jan 2000 – Dec 2018 for T	Moreo, 2015; Southern Nevada Water Authority (SNWA), 2019
1261	Lake Geneva	Europe	46.2, 6.2	370	156	571	T	/	Jan 2000 – Dec 2018	Tran Khac et al., 2018
1361	Lake Kasumigaura	East Asia	36.0, 140.5	0	7	168	E	EC	Jan 2008 – Dec 2012	Sugita et al., 2014
1381	Lake Biwa	East Asia	35.0, 135.9	81	42	673	T	/	Climatology	Ajioka et al., 2014
1414	Lake Kinneret	West Asia	33.69, 43.4	44	26	1699	E	BREB	Climatology (1986 – 2007)	Rimmer et al., 2009
9086	Lake Mendota	North America	43.1, -89.4	258	4.8	41	T	/	Jan 2000 – Nov 2007	Robertson, 2016
9475	Ross Barnett Reservoir	North America	32.5, -90.0	89	10.7	89	E	EC	Sep 2007 – Dec 2008	Liu et al., 2012
13962	Lake Ammersee	Europe	48.1, 11.13	531	16	45	T	/	May 2011 – Dec 2018	BLfU, 2019

observed temperature and/or evaporation rate data were available (Fig. 5 and Table 2). These 11 lakes are located on different continents and in various climate regions. They cover a good range of sizes, depths, and elevations, and thus are representative for testing the robustness of LTEM (Table 2). Among them, 4 of the lakes have eddy covariance (EC) evaporation rate measurements, and 2 have evaporation rate estimates using the BREB method. The EC method is regarded as the most accurate evaporation measurement technique (Friedrich et al., 2018). However, its expense has limited it from widespread application. In the BREB method, the heat storage change is addressed by measuring the temperature profiles. Although it is less accurate than the EC method, BREB has been widely employed due to its simplicity and reliability (Lenters et al., 2005b). In addition, 6 lakes with routinely monitored multi-depth temperature data were selected to validate the simulated temperature profiles. Among these lakes, Lake Mead has both EC evaporation rate and multi-depth temperature measurements, which makes it ideal for fully testing LTEM. Because these in-situ evaporation rate and temperature data are of different temporal resolutions, they were aggregated to monthly to be comparable with the simulated results.

In addition to the time-variant inputs (i.e., meteorological forcings and WST; Section 2.1) required to drive the model, LTEM also needs parameters such as lake bathymetry and the light attenuation coefficient (λ_{PAR}). The in-situ measured lake bathymetry data were collected from multiple sources for the 11 different lakes (Supplementary data Table S1). For large scale applications, coarse bathymetry data can be obtained using estimation methods such as those from Li et al. (2019), Li et al. (2020), Mu et al. (2020), Yigzaw et al. (2018), and Messager et al. (2016). Specifically, Li et al. (2020) developed a global reservoir bathymetry dataset for 347 of the world's reservoirs based on satellite radar/lidar data; and Messager et al. (2016) reported empirical depth-area relationships for 1.42 million lakes. Similarly, λ_{PAR} can be estimated using Equation 9 for large scale applications where only the depth data are available. In this study, we calculated λ_{PAR} from the in-situ measured Secchi depths (Supplementary data Table S1) using the logarithmic function (Equation 8). While LTEM supports the use of monthly λ_{PAR} values, we adopted a constant value for each lake in order to show the general applicability of the model. Results of sensitivity tests, and discussion about the uncertainty of λ_{PAR}, can be found in Sections 4.4 and 5.2, respectively.

4. Results

4.1. Lake surface area validation

The MODIS based lake surface area values were validated using the global surface water dataset (GSWD; Pekel et al., 2016). Based on Landsat imagery, GSWD provides monthly global water classifications (along with land and contaminated pixels) at 30 m resolution from March 1984 to December 2018. Here, only the lake areas from clear GSWD images were used to validate the enhanced MODIS image classifications.

Overall, the MODIS based lake surface area values agree well with those from GSWD (Fig. 6). The R^2 value is 0.99 for the 11 lakes, and the averaged relative bias is -2% (from -10% to 8% for individual lakes). In general, the algorithm performs better for the lakes with large area variations (e.g., Lake Mead and Lake Nasser). For the lakes with small area changes (e.g., Lake Taihu), the range of area variations from MODIS tends to be underestimated.

4.2. LTEM validations

4.2.1. Validation of temperature profile

In Fig. 7, the simulated water temperature profiles are compared with observed ones for 6 lakes: 1) Oneida Lake (HydroLAKES ID 770); 2) Lake Mead (ID 809); 3) Lake Biwa (ID 1381); 4) Lake Geneva (ID 1261); 5) Lake Mendota (ID 9086); and 6) Lake Ammersee (ID 13962).

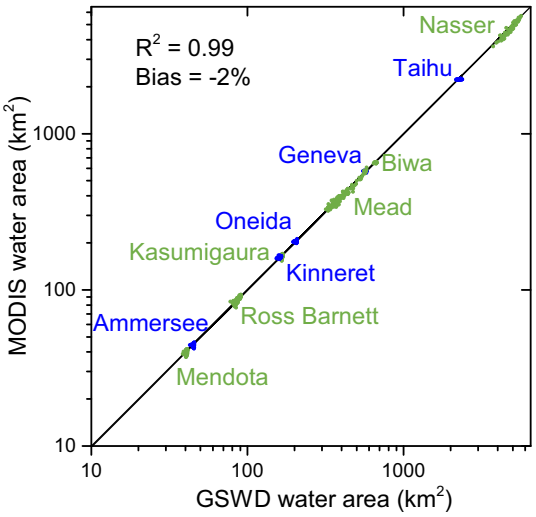

Fig. 6. Validation of MODIS-based lake surface areas using the high resolution Landsat-based lake surface area product. Different colors are used to distinguish between lakes whose area values are close to each other.

Overall, the simulated temperature profiles agree well with the observed ones. Validations of the average temperature profile (Columns a and b in Fig. 7) confirm the capability of LTEM to capture the seasonal variations of vertical thermal mixing for these lakes. For example, solar energy can penetrate to the bottom of Oneida Lake (Fig. 7-a1, b1) due to the shallow water depth (11 m). In contrast, for deep lakes such as Lake Mead (Fig. 7-a2, b2) and Lake Biwa (Fig. 7-a3, b3), the vertical thermal mixing depth varies by season. The underestimation of the deep water temperature of Lake Biwa is likely caused by the under-specification of the enhanced diffusion (κ_{en}) (Aota et al., 2006; Auger et al., 2013). To demonstrate the general applicability of LTEM, we used a universal value of 20 for α_{κ} to calculate κ_{en}. However, α_{κ} needs to be adjusted for water bodies like Lake Biwa which have strong turbulence.

Temperature values observed at multiple depths for each month were also used to validate the temperature profiles simulated by LTEM (Column c in Fig. 7). For the 5 lakes, the R^2 values are all greater than 0.9, the root mean square errors (RMSE) range from 1.1 °C to 1.8 °C, and the average biases range from -0.5 °C to 0.5 °C. This suggests that LTEM performs well at simulating the monthly dynamics of the temperature profiles (Antonopoulos and Gianniou, 2003). However, with regard to individual monthly value at a certain depth, the biases (simulated minus observed) can be large, ranging from -5.4 °C to 6.0 °C. These biases can be attributed to three sources of uncertainty: 1) MODIS WST data, 2) observed temperature data at multiple depths, and 3) model uncertainties. Because MODIS WST serves as the boundary condition for LTEM, its uncertainty (e.g., due to various weather conditions) can affect the temperature profile simulation results. Meanwhile, observed water temperatures are inclined toward uncertainties related to data collection times and locations. Like other physically-based numerical models, LTEM is susceptible to uncertainties from forcing inputs, parameters, and model structure (Ajami et al., 2007). In this study, it was found that the bulk temperature calculated from MODIS WST is biased from its in-situ counterpart (measured at 0.5 m) by -3.8 °C to 5.8 °C, which is similar to the total simulation bias range (i.e., -5.4 °C to 6.0 °C). Thus, we expect that the major sources of bias for the temperature profile are from observation and/or MODIS WST data, rather than from the model. Further discussion about these uncertainties can be found in Section 5.2.

4.2.2. Validation of evaporation rate

The simulated evaporation rate results were validated using either EC measurements or BREB estimates (Fig. 8 and Table 3). With the heat storage effect considered, the R^2 values range from 0.67 to 0.98. For each of the 6 lakes, the R^2 with the heat storage effect considered is higher than it is without (by 0.28 on average). This suggests that the seasonality of evaporation has been better represented. In particular, the largest improvements are observed for deep lakes, such as Lake Nasser (0.34 increase) and Lake Mead (0.44 increase). For Lake Taihu (average depth of 2.2 m), the improvement of R^2 is insignificant (0.03). This is because the heat storage changes are very small compared to the other energy terms for shallow lakes.

The absolute (relative) biases of the evaporation rates range from -0.19 mm/d (-8%) to 0.27 mm/d (9%) for the 6 lakes. However, apart from the R^2 measurement, the incorporation of heat storage simulation does not result in a notable improvement of the biases. This is because the heat storage is a seasonal phenomenon, and the errors tend to be canceled out in the annual average values. However, the RMSE values show significant improvement when the heat storage simulation is included. As with the R^2 values, the improvements of RMSE are generally larger for deeper lakes. For instance, the RMSE is reduced by 1.25 mm/d for Lake Kinneret (average depth of 26 m) while the reduction is only 0.12 mm/d for Lake Taihu (2.2 m). On average, the RMSE value has been reduced by 0.70 mm/d for these 6 lakes.

4.3. Evaporation losses from the lakes

Volumetric evaporation was calculated by multiplying the evaporation rate with the surface area (Equation 17). Using Lake Nasser as an example, Fig. 9 illustrates the time series of surface area, evaporation rate, and volumetric evaporation from 2000 to 2018 (as well as the seasonal cycles). With regard to surface area, it shows clear inter-annual and seasonal variabilities—both of which are consistent with the regional climate patterns (Gelete et al., 2019). For example, the decline of the surface area from 2002 to 2006 can be explained by the reduction of annual precipitation in the Nile Basin during this period (Awange et al., 2014). For each single year, the surface area typically decreases in the summer (due to limited precipitation in the upstream basins before June) and then increases after the rainy season (June to September).

The seasonality of the evaporation rate is mainly affected by the annual cycle of solar energy and the heat storage effect (Fig. 9b). Although the solar radiation generally peaks in June, the maximum values of evaporation rate (average 8.13 mm/d) usually occur in August—which is two months lagged due to the heat storage effect. The inter-annual and seasonal variabilities of volumetric evaporation are affected by both surface area and evaporation rate (Fig. 9c). For instance, volumetric evaporation shows low values in 2006 and 2012—which is consistent with the inter-annual changes of surface area. With respect to seasonality, volumetric evaporation peaks in September (1.08 km^3)—which results from a high evaporation rate and a relatively large surface area during this month. On average, the annual volumetric evaporation for Lake Nasser is 10.2 km^3, accounting for 6.3% of its storage capacity (162 km^3).

4.4. Parameter sensitivity

In LTEM, the simulated temperature profile—which directly affects the heat storage changes, and thus the evaporation rate—is sensitive to the light attenuation coefficient for PAR (λ_{PAR}) and to the enhanced diffusion coefficient (α_{κ}). In this study, time-invariant values of λ_{PAR} (calculated using the Secchi depth for each lake) and α_{κ} (equal to 20) have been used. To identify the effects of using these constants on the estimate of temperature profile and evaporation rate, two series of sensitivity tests were conducted using Lake Mead as an example. For λ_{PAR}, the simulations were conducted with values from 0.05 to 0.30 at an increment of 0.05; and for α_{κ} the sensitivity testing values were set between 0 to 200, depending on the mixing level.

Fig. 10 shows the sensitivities of the temperature profile and the

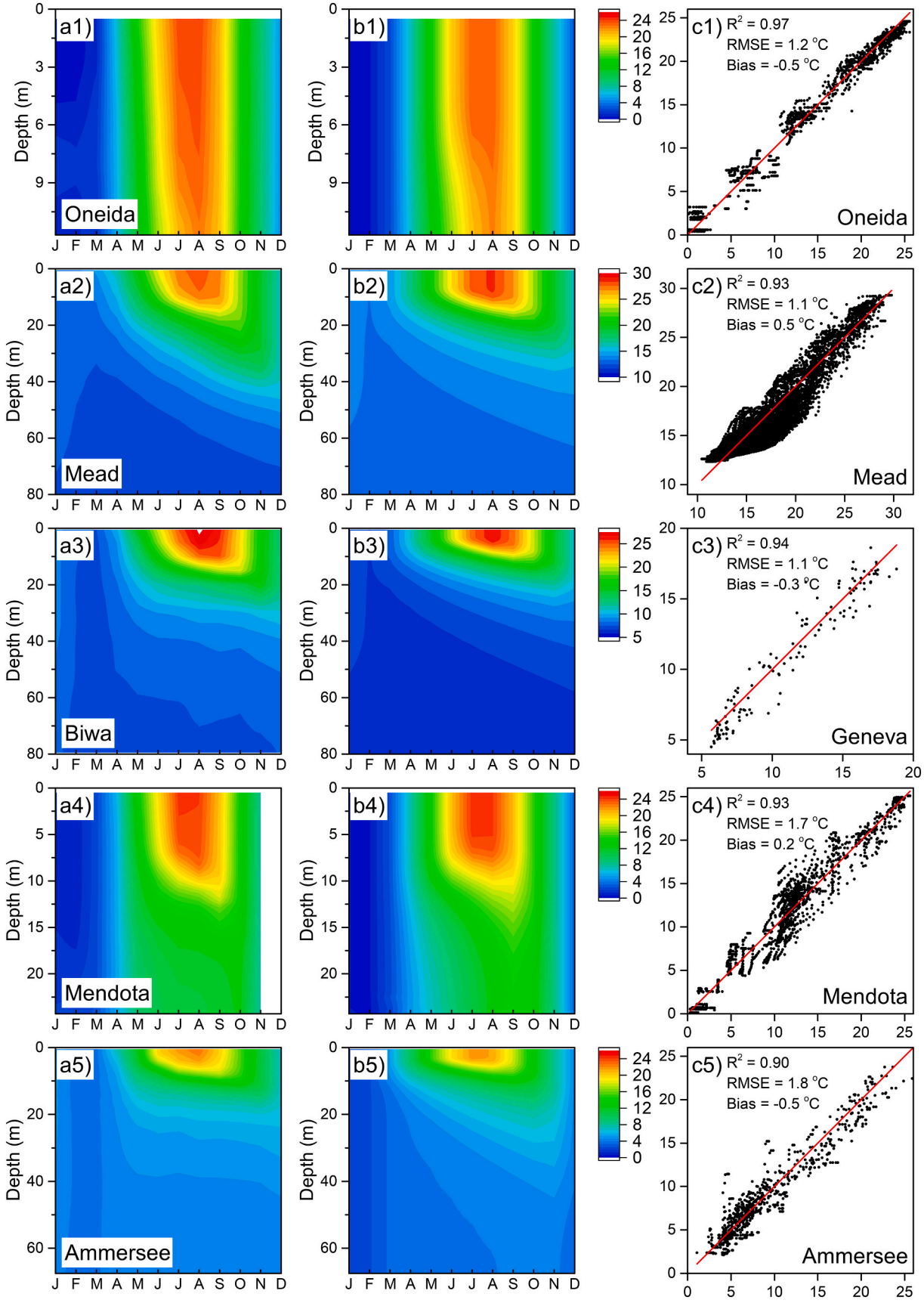

Fig. 7. Validation of temperature profiles simulated by LTEM against observed values for 6 lakes. Columns a and b show the climatological temperature profile for the observed and simulated data, while column c shows the comparisons of multi-depth temperature values for each month at each lake. For Lake Biwa, only the climatological temperature is shown due to data availability (a3 and b3). For Lake Geneva, only the monthly data comparison is shown (c3) because the observed temperatures are only reported as column-averaged values for the top 20 m.

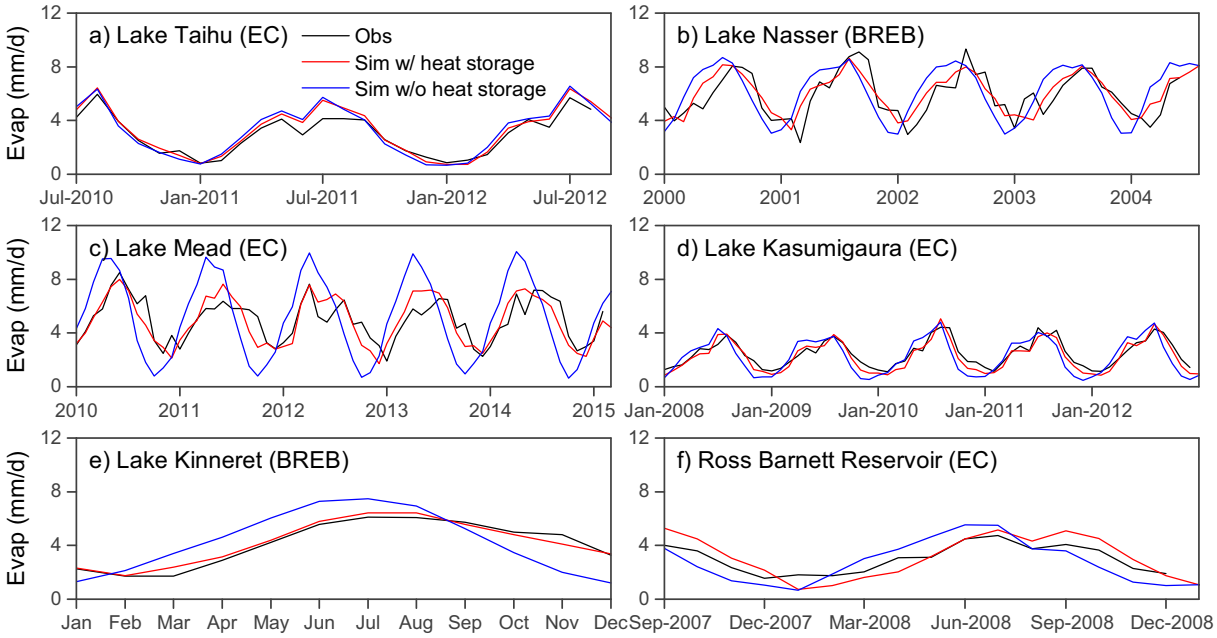

Fig. 8. Validation of the evaporation rate for 6 lakes with EC measurements or BREB estimates.

Table 3
Statistics of the evaporation rate simulation with and without the heat storage effect.

HydroLAKES ID	Lake	Depth	R^2 (with/without heat storage)	Absolute bias in mm/d (with/without heat storage)	Relative bias (with/without heat storage)	Root mean square error in mm/d (with/without heat storage)
148	Lake Taihu	2.2	0.96/0.93	0.27/0.28	9%/9%	0.49/0.61
152	Lake Nasser	30	0.67/0.33	0.14/0.25	2%/4%	0.96/1.67
809	Lake Mead	63	0.70/0.26	-0.02/0.22	-1%/4%	0.97/2.59
1361	Lake Kasumigaura	7	0.92/0.68	-0.19/-0.19	-8%/-8%	0.39/0.73
1414	Lake Kinneret	26	0.98/0.50	0.09/0.14	2%/3%	0.34/1.59
9475	Ross Barnett Reservoir	10.7	0.82/0.70	0.23/-0.16	8%/-5%	0.75/0.90

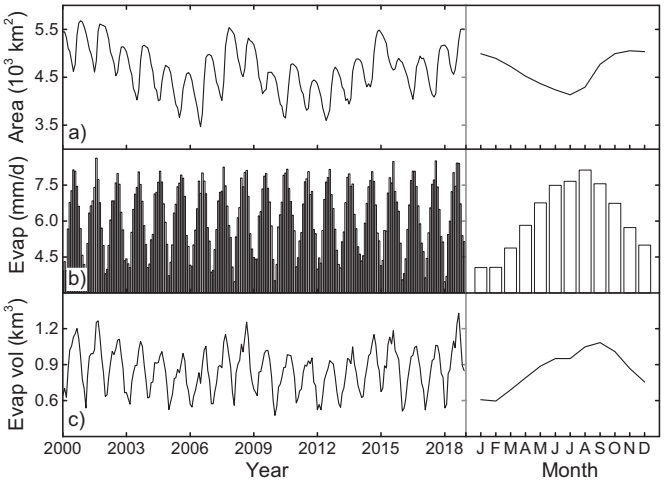

Fig. 9. Monthly time series and seasonality of a) surface area, b) evaporation rate, and c) volumetric evaporation for Lake Nasser, Egypt.

evaporation rate seasonality to these two parameters. With a smaller λ_{PAR} (i.e., a clearer water column), PAR can penetrate deeper into the water body (Fig. 10a). For instance, a value of 0.30 means that 90% of the PAR will be absorbed by the top 8 m of water, while this depth would be 46.5 m when λ_{PAR} equals 0.05. When the radiation energy can penetrate deeper, the evaporation on the water surface becomes more lagged in terms of the seasonality (Fig. 10b). For example, the evaporation rate peaks in July if λ_{PAR} is 0.30, and it peaks in September if λ_{PAR} is 0.05. α_κ mainly affects the heat conduction in the relatively deeper part of the water body (generally > 20 m). Fig. 10c suggests that with a larger α_κ, deep water mixing becomes more significant. The value of α_κ also impacts the evaporation seasonality (Fig. 10d). Similar to λ_{PAR}, a larger α_κ leads to deeper transmission of the radiation energy, resulting in a lagged evaporation rate.

5. Discussion

Accurate simulations of lake energy budgets and evaporation losses can benefit ecosystem protection, aquaculture management, and water resources planning. The results described above show that LTEM leveraged with MODIS WST data can be applied around the world to obtain more accurate estimates of lake temperature profiles and evaporation rates. Details regarding the algorithm's merits, uncertainties, and limitations, as well as some broader LTEM applications, are further discussed in this section.

5.1. Algorithm merits

A physically-based classification enhancement algorithm was adopted to overcome the limitations of MODIS image contaminations. Although the 8-day image composite algorithm can effectively improve image quality, water monitoring based on MODIS is still a challenging task due to frequent cloud contamination (Khandelwal et al., 2017; Klein et al., 2017). Compared to an earlier version developed for

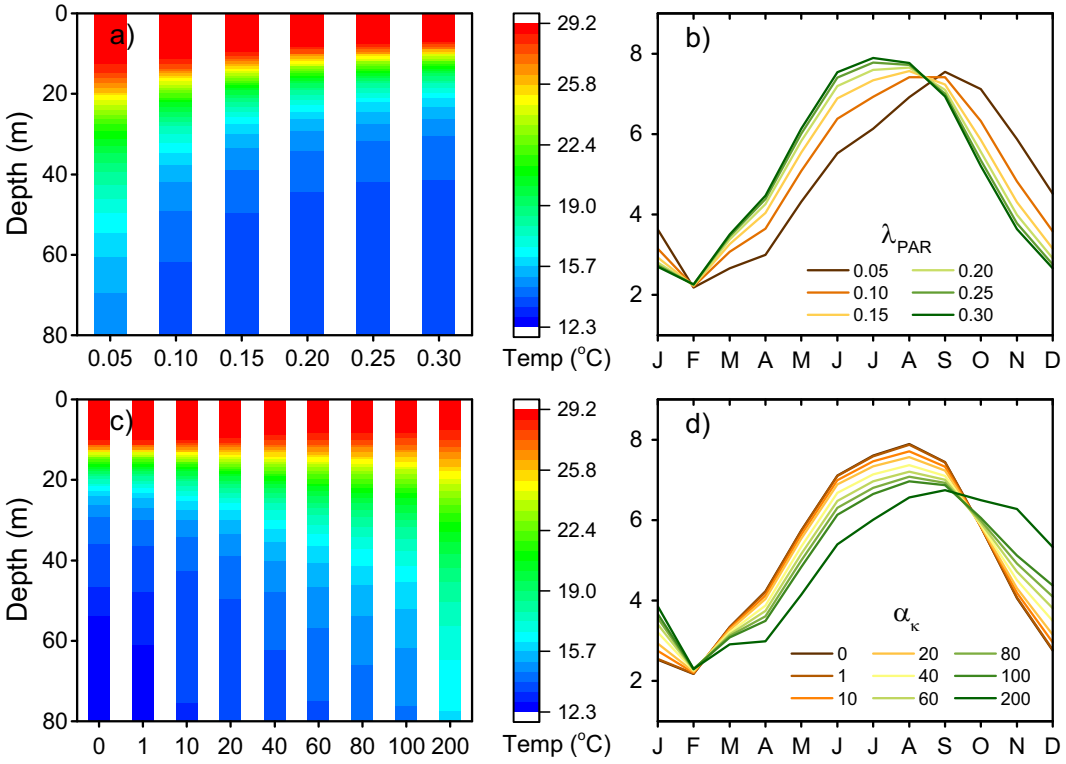

Fig. 10. a) Sensitivity of the temperature profile to the light attenuation coefficients for PAR (λ_{PAR}) and b) sensitivity of the evaporation rate to λ_{PAR}. c) and d) are same as a) and b) but for the enhanced diffusion coefficient (α_κ).

Landsat images (Zhao and Gao, 2018), this new algorithm does not rely on the use of an empirical parameter to calculate the occurrence threshold. Rather, it is similar to the method described in Yao et al. (2019), which expanded the visible coastlines into the cloudy areas through extrapolation. However, our algorithm implemented the expansion according to historical occurrence map, which is similar to a bathymetry map (Li et al., 2019). Therefore, our image enhancement approach is more physically based. The validation against Landsat classifications from clear images suggests that the algorithm and results are robust, despite the contaminations and the relatively coarse spatial resolution of MODIS images (Fig. 6).

By using the MODIS WST as the boundary condition of LTEM, the lake temperature profile can be simulated accurately. Similar to a Kalman Filter, MODIS WST can help to reduce the simulation uncertainty, which generally propagates with time (Samaniego et al., 2017). Results from six lakes across different continents (Fig. 7) show RMSE values of monthly temperature profiles that range from 1.1 °C to 1.8 °C; and long-term average biases that range from -0.5 °C to 0.5 °C. These results indicate good agreement between simulated and observed data in terms of both vertical thermal mixing and its seasonal variations (Perroud et al., 2009; Martynov et al., 2010). Benefiting from explicit temperature profile simulation, heat storage changes and evaporation rates were estimated with improved accuracy. As emphasized in Friedrich et al. (2018), the heat storage change is an important component for all energy-based evaporation estimation methods (e.g., Penman and BREB)—but it is difficult to obtain via either measurement or modeling methods. We have shown in this paper that LTEM can alleviate this issue. Compared to the bulk aerodynamic method that is commonly used in lake models (e.g., Bowling and Lettenmaier, 2010; Hipsey et al., 2019) for evaporation calculation, LTEM can provide better accuracy by explicitly incorporating heat storage simulations. Through the simulations, it was found that the heat storage effect reduces and delays the peak values in the monthly evaporation curves (Fig. 8). This effect is more significant for deep lakes (due to their large heat storage capacity) than for shallow lakes (Duan and Bastiaanssen, 2015; Zhao and Gao, 2019).

As discussed in several previous studies, the Hostetler Model tends to underestimate diffusive mixing—especially for deep lakes (Stepanenko et al., 2010; Martynov et al., 2010). This is likely due to additional turbulence introduced by sources not addressed in the model—such as surface inflow/outflow (notable in lakes with short residence times), seiches, the horizontal temperature gradient, and aquatic life movement (Fang and Stefan, 1996; Subin et al., 2012). This issue was also resolved in LTEM by adopting the enhanced diffusion scheme with a calibratable parameter (α_κ in Equation 13). Although we adopted a fixed value of α_κ (i.e., 20) for the lakes we tested, α_κ can be adjusted to unique values to achieve better thermal simulations for a specific lake. For instance, the underestimation of the deep mixing in Lake Biwa (Fig. 7-b3) can be mitigated by adopting a larger α_κ.

5.2. Algorithm uncertainties and limitations

The uncertainties associated with the final volumetric evaporation can be attributed to the uncertainties of surface area and evaporation rate—as well as to the preceding temperature profile, which determines the heat storage changes.

Although our image classification algorithm is advantageous in terms of raw image enhancement, uncertainties with regard to the area time series can originate from the Otsu thresholding step. Due to the low resolution (250 m) of MODIS, the Otsu method may misclassify mixed pixels (especially for lakes with large shoreline to area ratios; Gao et al., 2012), leading to biased area estimations (Jones and Sirault, 2014). This could further affect the accuracy of image enhancement, which uses the Otsu raw classifications as inputs. Although we used an occurrence threshold (Step 5 in Section 2.2) to alleviate such effects during enhancement, outliers may still exist in the time series for some lakes. Thus, the outlier removal process in Section 2.2 was designed to eliminate abnormal values (and thus can help to obtain high-quality

area time series values).

Sources of evaporation rate uncertainty mainly include forcing data uncertainty (Zhao and Gao, 2019) and model structure/parameter uncertainty (Fig. 10). Specifically, the forcing data used in this study (i.e., TerraClimate) is a land-based meteorological record (Abatzoglou et al., 2018). Although the increased humidity on the lake surface is represented by the wind function (McJannet et al., 2012; Zhao and Gao, 2019), differences in the wind speeds between lake and land regions are ignored—which might introduce some uncertainties (Schwab and Morton, 1984). In addition, the LTEM and its parameters can also produce uncertainties. For example, the formulation of the light attenuation coefficient (λ_{PAR}) is simplified using Equations 8 and 9. However, λ_{PAR} is affected by suspended solids, phytoplankton concentration level, and spectral distribution of solar radiation, and thus is constantly changing (Lee et al., 2005; Pinhassi et al., 2016). This limitation can possibly be alleviated using remotely sensed water quality products (Ritchie et al., 2003).

With regard to LTEM thermal simulation, the temperature profile biases can be attributed to several possible reasons. First, there are temporal inconsistencies between the observation data and the simulated results. Ideally, to calculate monthly/daily average temperatures, in-situ data need to be collected continuously in both daytime and nighttime. However, most monitoring sites report instantaneous measurements at a certain time of the day/month. For instance, the temperature data for Lake Mendota were mainly collected in the afternoon, while data for Lake Ammersee were reported only for the first 8 days in each month (BLfU, 2019). As a result, biases are introduced by ignoring diurnal and intra-monthly temperature changes (Vercauteren et al., 2011). Second, biases can also result from the uncertainties related to the WST data. Due to the intrinsic limitations of thermal infrared remote sensing, cloud contamination and weather conditions can notably impact the quality of the MODIS LST product (Wan, 2008). Meanwhile, the daytime LST is less accurate than the nighttime LST due to differential solar heating (Hook et al., 2003; Schneider et al., 2009). Third, the spatial representations of the observed temperature and the simulated temperature profiles are not exactly the same. Observation data were collected for a single water column (latitude and longitude), while the simulated data were averaged for the entire lake surface. Thus, the spatial heterogeneity caused by surface water currents can add biases to the validation results (Crosman and Horel, 2009).

There are two limitations of LTEM that are worth noting. First, the current version of LTEM does not consider the convective heat flux. For reservoirs whose inflow and outflow temperatures are significantly different, the convective energy flux can be large and thus affect the accuracy of the evaporation rate estimations (Huntington et al., 2014). Second, for the ice cover period, we assumed that there were no heat fluxes between the air and water, and there was no infiltration of shortwave radiation. The water temperature was simulated by only considering diffusion and convection (with the first layer temperature set to 0°C). This assumption might not be fully valid for cases in which there is only a very thin ice cover, and solar radiation can still penetrate through. Nonetheless, this simplification only has a limited impact on the evaporation rate, as evaporation from ice surfaces (i.e., ice sublimation) is close to zero.

5.3. Potential applications

Given the general availability of the meteorological forcings and of the MODIS WST data, LTEM can be employed to provide near real-time temperature profiles and evaporation information for lakes/reservoirs in any region around the world. This is expected to fill in a critical gap with regard to the current MODIS evapotranspiration product, in which evaporation from open water is not yet included. Furthermore, although a monthly time step was applied in this study, a shorter time step (e.g., daily) can be implemented with high temporal-resolution LST data. For instance, LST data from the Geostationary Operational Environmental Satellite (GOES) is provided every 3 hours at 4 km resolution, enabling diurnal simulations of the water temperature profiles for large lakes. Other promising LST products include Landsat-8 (16-day 30 m resolution), ECOSTRESS (2-4 days 70 m), and Sentinel-3 (2-day 1 km).

By adding more reliable volumetric evaporation data to the reservoir components of regional water management models (e.g., RiverWare; Zagona et al., 2001), water availability at the local, regional and continental scales can be estimated with improved accuracy (Maestre-Valero et al., 2013). Moreover, incorporating accurate volumetric evaporation information will provide a more accurate reservoir simulation module to watershed and regional hydrological models (Zhao et al., 2018) as well as to regional climate models (Mironov et al., 2010). This will improve the human dimension of climatic and hydrological models at various scales, and allow us to build more robust coupled nature-human system models (Vogel et al., 2015).

In addition, the temperature profiles from LTEM can be used to investigate lake thermal stratification, which is essential for improving water quality and ecosystem services (Antonopoulos and Gianniou, 2003). Under climate change and human interferences, thermal stability is especially important for understanding nutrient upwelling, lake eutrophication, and ecosystem service degradation for lakes across the world (Jankowski et al., 2006; Park et al., 2001).

6. Conclusion

An advanced framework has been developed in this study for an end-to-end quantification of volumetric lake evaporation. For lake surface area time series, we used the MODIS near-infrared and QA bands to develop a parameter-independent enhancement algorithm that reduces the impacts of image contamination on water classification. To better estimate heat storage changes, a new lake evaporation model—LTEM—was developed. Built upon the Hostetler Model, LTEM employs the MODIS WST as the boundary condition to provide a dynamic temperature profile, which is then used to quantify the heat storage changes and evaporation rate. To our best knowledge, this is the first time that the satellite measured skin temperature has been translated to a water column temperature profile, and then used to further facilitate quantification of the evaporation rate. The major conclusions of this study are summarized as follows:

1) By applying a classification enhancement algorithm, area estimations based on 250 m resolution MODIS near-infrared images can provide satisfactory information about lake area dynamics. Relative biases of the MODIS-based water areas range from -10% to 8% when compared to Landsat-based values.
2) Constrained by MODIS WST data, LTEM is capable of accurately simulating vertical thermal mixing and its seasonal variations. The long-term average temperature biases range from -0.5 °C to 0.5 °C. The biases of the monthly temperature profile range from -5.4 °C to 6.0 °C, which is mainly attributed to the uncertainties from WST and/or the observed temperature data.
3) By including explicit temperature profile simulation in LTEM, the heat storage change and the subsequent evaporation rate can be more accurately quantified than in existing methods. The average improvement of the R^2 values of the evaporation rates for the 6 lakes (after the heat storage simulations) is 0.28 and the average reduction of RMSE values is 0.70 mm/d.
4) Our proposed framework can support a broad spectrum of applications across spatiotemporal scales—including water resource management, lake ecological modeling, regional climate modeling, and global water cycle evaluations.

Author credit statement

Gang Zhao: Conceptualization, Methodology, Result Analysis,

Writing - Original Draft.

Huilin Gao: Conceptualization, Writing - Review & Editing, Supervision, Project Administration.

Ximing Cai: Writing - Review & Editing.

Declaration of Competing Interest

The authors whose names are listed immediately below certify that they have NO affiliations with or involvement in any organization or entity with any financial interest (such as honoraria; educational grants; participation in speakers' bureaus; membership, employment, consultancies, stock ownership, or other equity interest; and expert testimony or patent-licensing arrangements), or non-financial interest (such as personal or professional relationships, affiliations, knowledge or beliefs) in the subject matter or materials discussed in this manuscript.

Acknowledgment

This research was supported by the NASA Science of Terra, Aqua, and Suomi NPP (TASNPP) Program (80NSSC18K0939), and the Earth and Space Science Fellowship (NESSF) Program (80NSSC17K0358). It has benefitted from the usage of the Google Earth Engine platform and the Texas A&M Supercomputing Facility.

We would like to thank Dr. Todd Tietjen from the Southern Nevada Water Authority for providing the water temperature data for Lake Mead. We are thankful to Dr. Lars Rudstam from Cornell University for providing the water temperature monitoring time of Oneida Lake. We also thank Dr. Gideon Gal from Israel Oceanographic and Limnological Research for providing the water temperature data for Lake Kinneret.

Appendix A. Supplementary data

Supplementary data to this article can be found online at https://doi.org/10.1016/j.rse.2020.112104.

References

Abatzoglou, J.T., Dobrowski, S.Z., Parks, S.A., Hegewisch, K.C., 2018. TerraClimate, a high-resolution global dataset of monthly climate and climatic water balance from 1958–2015. Sci. Data 5, 170191.

Ajami, N.K., Duan, Q., Sorooshian, S., 2007. An integrated hydrologic Bayesian multi-model combination framework: Confronting input, parameter, and model structural uncertainty in hydrologic prediction. Water Resour. Res. 43.

Ajioka, T., Yamamoto, M., Murase, J., 2014. Branched and isoprenoid glycerol dialkyl glycerol tetraethers in soils and lake/river sediments in Lake Biwa basin and implications for MBT/CBT proxies. Org. Geochem. 73, 70–82.

Allen, R.G., Tasumi, M., 2005. Evaporation from American Falls Reservoir in Idaho via a combination of Bowen ratio and eddy covariance. Imp. Global Clim. Change 1–17.

Antonopoulos, V.Z., Gianniou, S.K., 2003. Simulation of water temperature and dissolved oxygen distribution in Lake Vegoritis, Greece. Ecol. Model. 160, 39–53.

Aota, Y., Kumagai, M., Kashiwaya, K., 2006. Estimation of vertical mixing based on water current monitoring in the hypolimnion of Lake Biwa. JSME Int. J. Ser. B Fluids Thermal Eng. 49, 621–625.

Artale, V., Iudicone, D., Santoleri, R., Rupolo, V., Marullo, S., D'Ortenzio, F., 2002. Role of surface fluxes in ocean general circulation models using satellite sea surface temperature: Validation of and sensitivity to the forcing frequency of the Mediterranean thermohaline circulation. J. Geophys. Res. Oceans 107 29-21-29-24.

Auger, G., Yamazaki, H., Nagai, T., Jiao, C., Kumagai, M., 2013. Hypolimnetic turbulence generation associated with superposition of large-scale internal waves in a strongly stratified lake: Lake Biwa, Japan. Limnology 14, 229–238.

Awange, J., Forootan, E., Kuhn, M., Kusche, J., Heck, B., 2014. Water storage changes and climate variability within the Nile Basin between 2002 and 2011. Adv. Water Resour. 73, 1–15.

Bayerisches Landesamt fur Umwelt (BLfU), 2019. Buoy water temperature for Lake Ammersee. available at: https://www.gkd.bayern.de/en/lakes/watertemperature accessed on: Aug 11, 2019.

Bennington, V., Notaro, M., Holman, K.D., 2014. Improving climate sensitivity of deep lakes within a regional climate model and its impact on simulated climate. J. Clim. 27, 2886–2911.

Blanken, P.D., Rouse, W.R., Culf, A.D., Spence, C., Boudreau, L.D., Jasper, J.N., Kochtubajda, B., Schertzer, W.M., Marsh, P., Verseghy, D., 2000. Eddy covariance measurements of evaporation from Great Slave lake, Northwest Territories, Canada. Water Resour. Res. 36, 1069–1077.

Blanken, P.D., Spence, C., Hedstrom, N., Lenters, J.D., 2011. Evaporation from Lake Superior: 1. Physical controls and processes. J. Great Lakes Res. 37, 707–716.

Bowling, L.C., Lettenmaier, D.P., 2010. Modeling the effects of lakes and wetlands on the water balance of Arctic environments. J. Hydrometeorol. 11, 276–295.

Brutsaert, W., Parlange, M., 1998. Hydrologic cycle explains the evaporation paradox. Nature 396, 30.

Carrea, L., Merchant, C.J., 2019. GloboLakes: Lake Surface Water Temperature (LSWT) v4.0 (1995-2016). Centre for Environmental Data Analysis. 29 March 2019. https://doi.org/10.5285/76a29c5b55204b66a40308fc2ba9cdb3.

Cavusoglu, A.-H., Chen, X., Gentine, P., Sahin, O., 2017. Potential for natural evaporation as a reliable renewable energy resource. Nat. Commun. 8, 617.

Chavula, G., Brezonik, P., Thenkabail, P., Johnson, T., Bauer, M., 2009. Estimating the surface temperature of Lake Malawi using AVHRR and MODIS satellite imagery. Physics Chem. Earth A/B/C 34, 749–754.

Coll, C., Wan, Z., Galve, J.M., 2009. Temperature-based and radiance-based validations of the V5 MODIS land surface temperature product. J. Geophys. Res.-Atmos. 114.

Crosman, E.T., Horel, J.D., 2009. MODIS-derived surface temperature of the Great Salt Lake. Remote Sens. Environ. 113, 73–81.

de Bruin, H., 1982. Temperature and energy balance of a water reservoir determined from standard weather data of a land station. J. Hydrol. 59, 261–274.

Devlin, M.J., Barry, J., Mills, D.K., Gowen, R.J., Foden, J., Sivyer, D., Tett, P., 2008. Relationships between suspended particulate material, light attenuation and Secchi depth in UK marine waters. Estuar. Coast. Shelf Sci. 79, 429–439.

Duan, Z., Bastiaanssen, W., 2015. A new empirical procedure for estimating intra-annual heat storage changes in lakes and reservoirs: review and analysis of 22 lakes. Remote Sens. Environ. 156, 143–156.

Ellis, C.R., Stefan, H.G., Gu, R., 1991. Water temperature dynamics and heat transfer beneath the ice cover of a lake. Limnol. Oceanogr. 36, 324–334.

Elsawwaf, M., Willems, P., Pagano, A., Berlamont, J., 2010. Evaporation estimates from Nasser Lake, Egypt, based on three floating station data and Bowen ratio energy budget. Theor. Appl. Climatol. 100, 439–465.

Escobedo, J.F., Gomes, E.N., Oliveira, A.P., Soares, J., 2009. Modeling hourly and daily fractions of UV, PAR and NIR to global solar radiation under various sky conditions at Botucatu, Brazil. Appl. Energy 86, 299–309.

Fairall, C., Bradley, E.F., Godfrey, J., Wick, G., Edson, J.B., Young, G.S., 1996. Cool-skin and warm-layer effects on sea surface temperature. J. Geophys. Res. Oceans 101, 1295–1308.

Fang, X., Stefan, H.G., 1996. Long-term lake water temperature and ice cover simulations/measurements. Cold Reg. Sci. Technol. 24, 289–304.

Finch, J., 2001. A comparison between measured and modelled open water evaporation from a reservoir in south-east England. Hydrol. Process. 15, 2771–2778.

Friedrich, K., Grossman, R.L., Huntington, J., Blanken, P.D., Lenters, J., Holman, K.D., Gochis, D., Livneh, B., Prairie, J., Skeie, E., 2018. Reservoir evaporation in the Western United States: current science, challenges, and future needs. Bull. Am. Meteorol. Soc. 99, 167–187.

Gao, H., Birkett, C., Lettenmaier, D.P., 2012. Global monitoring of large reservoir storage from satellite remote sensing. Water Resour. Res. 48 (9).

Gelete, G., Gokcekus, H., Gichamo, T., 2019. Impact of climate change on the hydrology of Blue Nile basin, Ethiopia: A review. J. Water Climate Change 14.

Gianniou, S.K., Antonopoulos, V.Z., 2007. Evaporation and energy budget in Lake Vegoritis, Greece. J. Hydrol. 345, 212–223.

Goudsmit, G.H., Burchard, H., Peeters, F., Wüest, A., 2002. Application of k-ϵ turbulence models to enclosed basins: The role of internal seiches. J. Geophys. Res. Oceans 107 23-21-23-13.

Håkanson, L., 1995. Models to predict Secchi depth in small glacial lakes. Aquat. Sci. 57, 31–53.

Haklay, M., Weber, P., 2008. Openstreetmap: User-generated street maps. IEEE Pervasive Comput. 7, 12–18.

Hamilton, D.P., Schladow, S.G., 1997. Prediction of water quality in lakes and reservoirs. Part I—Model description. Ecol. Model. 96, 91–110.

Hipsey, M.R., Bruce, L.C., Boon, C., Busch, B., Carey, C.C., Hamilton, D.P., Hanson, P.C., Read, J.S., De Sousa, E., Weber, M., 2019. A General Lake Model (GLM 3.0) for linking with high-frequency sensor data from the Global Lake Ecological Observatory Network (GLEON).

Hook, S.J., Prata, F.J., Alley, R.E., Abtahi, A., Richards, R.C., Schladow, S.G., Pálmarsson, S., 2003. Retrieval of lake bulk and skin temperatures using Along-Track Scanning Radiometer (ATSR-2) data: A case study using Lake Tahoe, California. J. Atmos. Ocean. Technol. 20, 534–548.

Horrocks, L.A., Candy, B., Nightingale, T.J., Saunders, R.W., O'Carroll, A., Harris, A.R., 2003. Parameterizations of the ocean skin effect and implications for satellite-based measurement of sea-surface temperature. J. Geophys. Res. Oceans 108 (C3).

Hostetler, S., Bartlein, P., 1990. Simulation of lake evaporation with application to modeling lake level variations of Harney-Malheur Lake, Oregon. Water Resour. Res. 26, 2603–2612.

Huntington, J., Gangopadhyay, S., King, D., Morton, C., Spears, M., Allen, R., Joros, A., 2014. West-wide climate risk assessments: bias-corrected and spatially downscaled irrigation demand and reservoir evaporation projections. Technical Memorandum 01.

Ingle Jr., J.D., Crouch, S.R., 1988. Spectrochemical analysis. United States.

Jankowski, T., Livingstone, D.M., Bührer, H., Forster, R., Niederhauser, P., 2006. Consequences of the 2003 European heat wave for lake temperature profiles, thermal stability, and hypolimnetic oxygen depletion: Implications for a warmer world. Limnol. Oceanogr. 51, 815–819.

Jones, H., Sirault, X., 2014. Scaling of thermal images at different spatial resolution: the mixed pixel problem. Agronomy 4, 380–396.

Khandelwal, A., Karpatne, A., Marlier, M.E., Kim, J., Lettenmaier, D.P., Kumar, V., 2017. An approach for global monitoring of surface water extent variations in reservoirs

using MODIS data. Remote Sens. Environ. 202, 113–128.
Kirillin, G., Hochschild, J., Mironov, D., Terzhevik, A., Golosov, S., Nützmann, G., 2011. FLake-Global: Online lake model with worldwide coverage. Environ. Model Softw. 26, 683–684.
Klein, I., Gessner, U., Dietz, A.J., Kuenzer, C., 2017. Global WaterPack–A 250 m resolution dataset revealing the daily dynamics of global inland water bodies. Remote Sens. Environ. 198, 345–362.
Lee, Z.P., Darecki, M., Carder, K.L., Davis, C.O., Stramski, D., Rhea, W.J., 2005. Diffuse attenuation coefficient of downwelling irradiance: An evaluation of remote sensing methods. J. Geophys. Res. Oceans 110.
Lenters, J.D., Kratz, T.K., Bowser, C.J., 2005a. Effects of climate variability on lake evaporation: Results from a long-term energy budget study of Sparkling Lake, northern Wisconsin (USA). J. Hydrol. 308, 168–195.
Lenters, J.D., Kratz, T.K., Bowser, C.J., 2005b. Effects of climate variability on lake evaporation: Results from a long-term energy budget study of Sparkling Lake, northern Wisconsin (USA). J. Hydrol. 308, 168–195.
Li, Y., Gao, H., Jasinski, M.F., Zhang, S., Stoll, J.D., 2019. Deriving high-resolution reservoir bathymetry from ICESat-2 prototype photon-counting Lidar and Landsat imagery. IEEE Trans. Geosci. Remote Sens. 57, 7883–7893.
Li, Y., Gao, H., Zhao, G., Tseng, K.-H., 2020. A high-resolution bathymetry dataset for global reservoirs using multi-source satellite imagery and altimetry. Remote Sens. Environ. 244, 111831.
Linacre, E.T., 1993. Data-sparse estimation of lake evaporation, using a simplified Penman equation. Agric. For. Meteorol. 64, 237–256.
Liu, H., Zhang, Q., Dowler, G., 2012. Environmental controls on the surface energy budget over a large southern inland water in the United States: An analysis of one-year eddy covariance flux data. J. Hydrometeorol. 13, 1893–1910.
Lu, S., Jia, L., Zhang, L., Wei, Y., Baig, M.H.A., Zhai, Z., Meng, J., Li, X., Zhang, G., 2017. Lake water surface mapping in the Tibetan Plateau using the MODIS MOD09Q1 product. Remote Sens. Lett. 8, 224–233.
MacCallum, S.N., Merchant, C.J., 2012. Surface water temperature observations of large lakes by optimal estimation. Can. J. Remote. Sens. 38, 25–45.
Maestre-Valero, J., Martínez-Granados, D., Martínez-Alvarez, V., Calatrava, J., 2013. Socio-economic impact of evaporation losses from reservoirs under past, current and future water availability scenarios in the semi-arid Segura Basin. Water Resour. Manag. 27, 1411–1426.
Martynov, A., Sushama, L., Laprise, R., 2010. Simulation of temperate freezing lakes by one-dimensional lake models: performance assessment for interactive coupling with regional climate models.
McJannet, D., Webster, I., Stenson, M., Sherman, B., 2008. Estimating open water evaporation for the Murray-Darling Basin. CSIRO, Water for a Healthy Country National Research Flagship.
McJannet, D.L., Webster, I.T., Cook, F.J., 2012. An area-dependent wind function for estimating open water evaporation using land-based meteorological data. Environ. Model Softw. 31, 76–83.
McMahon, T., Peel, M., Lowe, L., Srikanthan, R., McVicar, T., 2013. Estimating actual, potential, reference crop and pan evaporation using standard meteorological data: a pragmatic synthesis. Hydrol. Earth Syst. Sci. 17, 1331–1363.
McVicar, T.R., Roderick, M.L., Donohue, R.J., Li, L.T., Van Niel, T.G., Thomas, A., Grieser, J., Jhajharia, D., Himri, Y., Mahowald, N.M., 2012. Global review and synthesis of trends in observed terrestrial near-surface wind speeds: Implications for evaporation. J. Hydrol. 416, 182–205.
Messager, M.L., Lehner, B., Grill, G., Nedeva, I., Schmitt, O., 2016. Estimating the volume and age of water stored in global lakes using a geo-statistical approach. Nat. Commun. 7, 1–11.
Mironov, D., Heise, E., Kourzeneva, E., Ritter, B., Schneider, N., Terzhevik, A., 2010. Implementation of the lake parameterisation scheme FLake into the numerical weather prediction model COSMO.
Monteith, J.L., 1965. Evaporation and environment. In, Symposia of the Society for Experimental Biology (p. 4).
Moreo, M., 2015. Evaporation data from Lake Mead and Lake Mohave, Nevada and Arizona, March 2010 through April 2015. US Geological Survey. https://doi.org/10.5066/F79C6VG3.
Morton, F.I., 1983. Operational estimates of areal evapotranspiration and their significance to the science and practice of hydrology. J. Hydrol. 66, 1–76.
Mu, M., Tang, Q., Han, S., Liu, X., Cui, H., 2020. Using GRanD Database and Surface Water Data to Constrain Area–Storage Curve of Reservoirs. Water 12, 1242.
Otsu, N., 1979. A threshold selection method from gray-level histograms. IEEE Trans. Syst. Man Cybern. 9, 62–66.
Park, H.D., Sasaki, Y., Maruyama, T., Yanagisawa, E., Hiraishi, A., Kato, K., 2001. Degradation of the cyanobacterial hepatotoxin microcystin by a new bacterium isolated from a hypertrophic lake. Environ. Toxicol. 16, 337–343.
Pekel, J.-F., Cottam, A., Gorelick, N., Belward, A.S., 2016. High-resolution mapping of global surface water and its long-term changes. Nature 540, 418–422.
Penman, H.L., 1948. Natural evaporation from open water, bare soil and grass. In, Proceedings of the Royal Society of London A: Mathematical, Physical and Engineering Sciences (pp. 120-145): The Royal Society.
Perroud, M., Goyette, S., Martynov, A., Beniston, M., Annevillec, O., 2009. Simulation of multiannual thermal profiles in deep Lake Geneva: A comparison of one-dimensional lake models. Limnol. Oceanogr. 54, 1574–1594.
Pinhassi, J., DeLong, E.F., Béjà, O., González, J.M., Pedrós-Alió, C., 2016. Marine bacterial and archaeal ion-pumping rhodopsins: genetic diversity, physiology, and ecology. Microbiol. Mol. Biol. Rev. 80, 929–954.
Priestley, C., Taylor, R., 1972. On the assessment of surface heat flux and evaporation using large-scale parameters. Mon. Weather Rev. 100, 81–92.
Rimmer, A., Samuels, R., Lechinsky, Y., 2009. A comprehensive study across methods and time scales to estimate surface fluxes from Lake Kinneret, Israel. J. Hydrol. 379, 181–192.
Ritchie, J.C., Zimba, P.V., Everitt, J.H., 2003. Remote sensing techniques to assess water quality. Photogramm. Eng. Remote Sens. 69, 695–704.
Robertson, D.M., 2016. Lake Mendota water temperature secchi depth snow depth ice thickness and meterological conditions 1894 - 2007, available at. https://lter.limnology.wisc.edu/.
Rudstam, L.G., 2015. Limnological data and depth profile from Oneida Lake, New York, 1975 to present. available at: https://hdl.handle.net/1813/11229.
Samaniego, L., Kumar, R., Breuer, L., Chamorro, A., Flörke, M., Pechlivanidis, I.G., Schäfer, D., Shah, H., Vetter, T., Wortmann, M., 2017. Propagation of forcing and model uncertainties on to hydrological drought characteristics in a multi-model century-long experiment in large river basins. Clim. Chang. 141, 435–449.
Schneider, P., Hook, S., Radocinski, R., Corlett, G., Hulley, G., Schladow, S., Steissberg, T., 2009. Satellite observations indicate rapid warming trend for lakes in California and Nevada. Geophys. Res. Lett. 36.
Schwab, D.J., Morton, J.A., 1984. Estimation of overlake wind speed from overland wind speed: A comparison of three methods. J. Great Lakes Res. 10, 68–72.
Sharma, S., Gray, D.K., Read, J.S., O'Reilly, C.M., Schneider, P., Qudrat, A., Gries, C., Stefanoff, S., Hampton, S.E., Hook, S., 2015. A global database of lake surface temperatures collected by in situ and satellite methods from 1985–2009. Sci. Data 2, 150008.
Sima, S., Ahmadalipour, A., Tajrishy, M., 2013. Mapping surface temperature in a hypersaline lake and investigating the effect of temperature distribution on the lake evaporation. Remote Sens. Environ. 136, 374–385.
Song, K., Wang, M., Du, J., Yuan, Y., Ma, J., Wang, M., Mu, G., 2016. Spatiotemporal variations of lake surface temperature across the Tibetan Plateau using MODIS LST product. Remote Sens. 8, 854.
Southern Nevada Water Authority (SNWA), 2019. Buoy water temperature for Lake Mead at station CR346.4, available at. https://www.snwa.com/ accessed on: Aug 11, 2019.
Stannard, D.I., Rosenberry, D.O., 1991. A comparison of short-term measurements of lake evaporation using eddy correlation and energy budget methods. J. Hydrol. 122, 15–22.
Stepanenko, V.M., Goyette, S., Martynov, A., Perroud, M., Fang, X., Mironov, D., 2010. First steps of a lake model intercomparison Project: LakeMIP.
Stepanenko, V., Martynov, A., Jöhnk, K., Subin, Z., Perroud, M., Fang, X., Beyrich, F., Mironov, D., Goyette, S., 2013. A one-dimensional model intercomparison study of thermal regime of a shallow, turbid midlatitude lake. Geosci. Model Dev. 6, 1337–1352.
Subin, Z.M., Riley, W.J., Mironov, D., 2012. An improved lake model for climate simulations: Model structure, evaluation, and sensitivity analyses in CESM1. J. Adv. Model. Earth Syst. 4.
Sugita, M., Ikura, H., Miyano, A., Yamamoto, K., Zhongwang, W., 2014. Evaporation from Lake Kasumigaura: annual totals and variability in time and space. Hydrol. Res. Lett. 8, 103–107.
Terzi, Ö., Erol Keskin, M., Dilek Taylan, E., 2006. Estimating evaporation using ANFIS. J. Irrig. Drain. Eng. 132, 503–507.
Tran Khac, V., Anneville, O., Barbet, D., Clément, J.-C., Domaizon, I., Dorioz, J.-M., Frossard, V., Guillard, J., Hustache, J.-C., Jacquet, S., Perney, P., Quetin, P., Rimet, F., Monet, G., 2018. Lake surface water temperature of Lake Geneva, Lake Bourget, Lake Annecy and Lake Aiguebelette. In: Portail Data Inra.
Tu, C.Y., Tsuang, B.J., 2005. Cool-skin simulation by a one-column ocean model. Geophys. Res. Lett. 32.
Valiantzas, J.D., 2006. Simplified versions for the Penman evaporation equation using routine weather data. J. Hydrol. 331, 690–702.
Vallet-Coulomb, C., Legesse, D., Gasse, F., Travi, Y., Chernet, T., 2001. Lake evaporation estimates in tropical Africa (Lake Ziway, Ethiopia). J. Hydrol. 245, 1–18.
Vercauteren, N., Huwald, H., Bou-Zeid, E., Selker, J.S., Lemmin, U., Parlange, M.B., Lunati, I., 2011. Evolution of superficial lake water temperature profile under diurnal radiative forcing. Water Resour. Res. 47.
Vermote, E., Kotchenova, S., & Ray, J. (2015). MODIS surface reflectance user's guide. MODIS Land Surface Reflectance Science Computing Facility, version 1.4.
Vickers, D., Mahrt, L., Andreas, E.L., 2015. Formulation of the sea surface friction velocity in terms of the mean wind and bulk stability. J. Appl. Meteorol. Climatol. 54, 691–703.
Vogel, R.M., Lall, U., Cai, X., Rajagopalan, B., Weiskel, P.K., Hooper, R.P., Matalas, N.C., 2015. Hydrology: The interdisciplinary science of water. Water Resour. Res. 51, 4409–4430.
Wan, Z., 2008. New refinements and validation of the MODIS land-surface temperature/emissivity products. Remote Sens. Environ. 112, 59–74.
Wan, Z., 2014. New refinements and validation of the collection-6 MODIS land-surface temperature/emissivity product. Remote Sens. Environ. 140, 36–45.
Wan, W., Li, H., Xie, H., Hong, Y., Long, D., Zhao, L., Han, Z., Cui, Y., Liu, B., Wang, C., 2017. A comprehensive data set of lake surface water temperature over the Tibetan Plateau derived from MODIS LST products 2001–2015. Sci. Data 4, 170095.
Wang, K., Wan, Z., Wang, P., Sparrow, M., Liu, J., Haginoya, S., 2007. Evaluation and improvement of the MODIS land surface temperature/emissivity products using ground-based measurements at a semi-desert site on the western Tibetan Plateau. Int. J. Remote Sens. 28, 2549–2565.
Wang, W., Xiao, W., Cao, C., Gao, Z., Hu, Z., Liu, S., Shen, S., Wang, L., Xiao, Q., Xu, J., 2014. Temporal and spatial variations in radiation and energy balance across a large freshwater lake in China. J. Hydrol. 511, 811–824.
Wang, W., Lee, X., Xiao, W., Liu, S., Schultz, N., Wang, Y., Zhang, M., Zhao, L., 2018. Global lake evaporation accelerated by changes in surface energy allocation in a warmer climate. Nat. Geosci. 11, 410–414.
Wozniak, B., Dera, J., 2007. Light absorption by water molecules and inorganic

substances dissolved in sea water. Light Absorption in Sea Water, 11-81.
Wurbs, R.A., Ayala, R.A., 2014. Reservoir evaporation in Texas, USA. J. Hydrol. 510, 1–9.
Yao, F., Wang, J., Wang, C., Crétaux, J.-F., 2019. Constructing long-term high-frequency time series of global lake and reservoir areas using Landsat imagery. Remote Sens. Environ. 232, 111210.
Yigzaw, W., Li, H.Y., Demissie, Y., Hejazi, M.I., Leung, L.R., Voisin, N., Payn, R., 2018. A new global storage-area-depth data set for modeling reservoirs in land surface and Earth system models. Water Resour. Res. 54, 10,372–310,386.
Zagona, E.A., Fulp, T.J., Shane, R., Magee, T., Goranflo, H.M., 2001. Riverware: A generalized tool for complex reservoir system modeling 1. JAWRA J. Am. Water Resources Assoc. 37, 913–929.
Zhang, S., Pavelsky, T.M., 2019. Remote Sensing of Lake Ice Phenology across a Range of Lakes Sizes, ME, USA. Remote Sens. 11, 1718.
Zhang, S., Gao, H., Naz, B.S., 2014. Monitoring reservoir storage in South Asia from multisatellite remote sensing. Water Resour. Res. 50, 8927–8943.
Zhao, G., Gao, H., 2018. Automatic correction of contaminated images for assessment of reservoir surface area dynamics. Geophys. Res. Lett. 45, 6092–6099.
Zhao, G., Gao, H., 2019. Estimating reservoir evaporation losses for the United States: Fusing remote sensing and modeling approaches. Remote Sens. Environ. 226, 109–124.
Zhao, G., Gao, H., Kao, S.-C., Voisin, N., Naz, B.S., 2018. A modeling framework for evaluating the drought resilience of a surface water supply system under non-stationarity. J. Hydrol. 563, 22–32.